




## ARTICLE OPEN



# Switch to phagocytic microglia by CSFR1 inhibition drives amyloid-beta clearance from glutamatergic terminals rescuing LTP in acute hippocampal slices

Gaia Piccioni<sup>1,2</sup>, Nunzia Maisto<sup>1,2</sup>, Asia d'Ettore<sup>3,4</sup>, Georgios Strimpakos<sup>3</sup>, Robert Nistico<sup>1,4</sup>, Viviana Triaca<sup>3,5</sup> and Dalila Mango<sup>1,4,5</sup>

© The Author(s) 2024

Microglia, traditionally regarded as innate immune cells in the brain, drive neuroinflammation and synaptic dysfunctions in the early phases of Alzheimer disease (AD), acting upstream to A $\beta$  accumulation. Colony stimulating factor 1-receptor (CSF-1R) is predominantly expressed on microglia and its levels are significantly increased in neurodegenerative diseases, possibly contributing to the chronic inflammatory microglial response. On the other hand, CSF-1R inhibitors confer neuroprotection in preclinical models of neurodegenerative diseases. Here, we determined the effects of the CSF-1R inhibitor PLX3397 on the A $\beta$ -mediated synaptic alterations in ex vivo hippocampal slices. Electrophysiological findings show that PLX3397 rescues LTP impairment and neurotransmission changes induced by A $\beta$ . In addition, using confocal imaging experiments, we demonstrate that PLX3397 stimulates a microglial transition toward a phagocytic phenotype, which in turn promotes the clearance of A $\beta$  from glutamatergic terminals. We believe that the selective pruning of A $\beta$ -loaded synaptic terminals might contribute to the restoration of LTP and excitatory transmission alterations observed upon acute PLX3397 treatment. This result is in accordance with the mechanism proposed for CSF1R inhibitors, that is to eliminate responsive microglia and replace it with newly generated, homeostatic microglia, capable of promoting brain repair. Overall, our findings identify a connection between the rapid microglia adjustments and the early synaptic alterations observed in AD, possibly highlighting a novel disease-modifying target.

*Translational Psychiatry* (2024)14:338; <https://doi.org/10.1038/s41398-024-03019-2>

## INTRODUCTION

Microglia exert a crucial role in synaptic plasticity [1, 2] and pruning functions during development and adulthood [3, 4], when they promote local neuronal network synchronization [5], and reorganization during brain repair [6]. Microglia are the brain resident immune cells and dynamically perform different key functions, including innate immune functions, surveillance of local microenvironment, coordination with astrocytes, and regulation of myelin homeostasis [7–14]. Surveillant microglia are highly dynamic and context-dependent heterogeneous cells [15] and react to their *milieu* through specific patterns of concurring morphological, metabolic and spatial adaptations [16, 17] to maintain the brain homeostasis in physiological conditions as well as in neurodegenerative disorders, such as Alzheimer's disease (AD).

Microglia may exert both beneficial and harmful effects in AD [18]. During early phase AD, protection against toxic aggregated proteins occurs by surveillant microglia that switch to a phagocytic profile [18–20]. On the other hand, late phase of AD is characterized by pathological microgliopathy, with overreactive microglia proliferating and releasing cytokines that amplify the

neuroinflammatory process caused by cytotoxic oligomerization of  $\beta$ -amyloid (A $\beta$ ) and tau, finally leading to synaptic damage and cognitive deficits [21–24]. In particular, the soluble oligomeric form of A $\beta$  (oA $\beta$ ) has the main impact on early synaptic dysfunction [25], being a better correlate of impaired synaptic plasticity and cognitive decline than the insoluble amyloid pool [26]. Moreover, soluble oA $\beta$  may provide a mechanism for early AD memory loss [27] also in the absence of plaque pathology in AD [28].

AD is a major neurodegenerative disorder characterized by a progressive deterioration of memory performance, cognitive decline, and behavioral alterations but its etiopathology is still under debate [25]. Genome-wide association studies (GWAS) of late-onset sporadic AD showed that aggregated instead of single gene mutations have causal effects on disease susceptibility, hence validating the hypothesis of a multifactorial nature of the disease [29]. Interestingly, the majority of the over 50 AD-linked loci identified by GWAS were associated with genes highly or exclusively expressed by microglia [30]. In particular, an association between the variants of Colony stimulating factor 1 receptor (CSF1R) and the AD risk was found [31–33]. CSF1R and its ligand

<sup>1</sup>Laboratory Pharmacology of Synaptic Plasticity, European Brain Research Institute, Rome, Italy. <sup>2</sup>Department of Physiology and Pharmacology "V. Erspamer", Sapienza University of Rome, Rome, Italy. <sup>3</sup>Institute of Biochemistry and Cell Biology, National Research Council (CNR), International Campus A. Buzzati-Traverso, Rome, Italy. <sup>4</sup>School of Pharmacy, University of Rome "Tor Vergata", Rome, Italy. <sup>5</sup>These authors contributed equally: Viviana Triaca, Dalila Mango. <sup>✉</sup>email: robert.nistico@uniroma2.it; viviana.triaca@cnr.it; dalila.mango@uniroma2.it

CSF1 are main players of microglial development, survival, and metabolism [34] as well as crucial orchestrators of the inflammatory response in AD and other neurodegenerative disorders [35]. Noteworthy, the reduction of intraneuronal amyloid and plaque deposition, and amelioration of cognitive function upon treatment of 5XFAD mice with the CSF1R inhibitor PLX3397 suggests a crucial role of CSF1R in AD pathology [36] and supports the use of CSF1R inhibitors in AD therapy [30]. Notably, depending on the dose and timing and administration route, CSF1R inhibitors can either deplete microglia or modify their metabolism, morphology and function [37, 38]. However, caution should be taken when affecting CSF1R signaling in microglia by systemic CSF1R inhibitors. In fact, CSF1R expression is not restricted to brain resident microglia and its precursors [39], but it is present in several tissues and cell types, like neurons [40–42], neural progenitor cells [41], and capillary endothelial cells in the CNS [43]. As expected, the effect on microglia and synaptic plasticity patterns are quite dramatic, with microglia depletion and repopulation from peripheral macrophages in constitutive global *csf1r*<sup>-/-</sup> mice and mice subjected to long-term systemic CSF1R inhibitors [44, 45]. Also, they are far different from the microglia modulation in absence of cell death described in the more physiological paradigms of CSF1R haploinsufficient, CSF1R hypomorphic and microglial conditional CSF1R KO mice [45–47], thus claiming for off-target effects of systemic CSF1R inhibition.

To avoid these limitations, while studying microglia behavior in an intact hippocampal network, here we resorted to CSF1R inhibition by PLX3397 administration to acute hippocampal slices exposed to soluble oligomeric A $\beta$ <sub>1–42</sub> (A $\beta$ <sub>1–42</sub>) [48]. We performed electrophysiological and confocal imaging analysis of microglial morphology by means of key functional markers and found that PLX3397 boosts phagocytic microglia and promotes the clearance of A $\beta$ <sub>1–42</sub> from glutamatergic terminals in the hippocampus, finally resulting in normalization of glutamatergic transmission and recovery of A $\beta$ -mediated LTP impairments.

Considering this evidence, low grade CSF1R inhibition by PLX3397 in hippocampal slices represents a valid experimental tool to investigate the rapid microglia behavior in the hippocampal network and possibly identify new therapeutic strategies of relevance for AD neurodegeneration.

## MATERIALS AND METHODS

### Animals

All animals were handled in compliance with the national (D.Lgs 26/2014) and international guidelines for animal welfare (European Communities Council Directive 2010/63/EU). All efforts were approved by appropriate institutional and state authorities of EBRI Rita Levi-Montalcini Foundation (F8BDD.N.IAY). In compliance to the Italian law and EU directives, all efforts were made to minimize the number of animals used and suffering according to the principle of 3Rs. Animal studies are reported in compliance with the ARRIVE guidelines [49]. C57/Bl6J mice were housed at the EBRI Rita Levi-Montalcini Foundation (Rome, Italy).

### Slice preparation

Parasagittal hippocampal slices (250–400  $\mu$ m) from C57Bl6/J were obtained as described in detail previously [48, 49].

The slices for field extracellular recordings were incubated for 30 min before recording with A $\beta$ <sub>1–42</sub> (200 nM), in whole cell patch clamp recordings A $\beta$ <sub>1–42</sub> (500 nM) was perfused for 10 min [50]. As control, A $\beta$ <sub>scrambled</sub> was applied at the same time and concentration of A $\beta$ <sub>1–42</sub>. In minocycline group, the slices were incubated with minocycline (500 nM) for 30 min alone or in co-incubation with A $\beta$ <sub>1–42</sub>, then minocycline was perfused for 1 h during the recording. PLX3397 (10  $\mu$ M, PLX) was applied for 30 min alone or with A $\beta$ <sub>1–42</sub> and perfused during baseline recording.

Electrophysiological recordings on treated slices were started within 30 min after the end of treatment.

Immunofluorescence was performed on hippocampal slices fixed with 4% PFA immediately after the pharmacological treatment.

### Electrophysiology

Extracellular field recordings were performed for the LTP experiments using a stimulating electrode placed in *stratum radiatum* to stimulate Schaffer Collateral pathway and LTP was induced using Theta Burst Stimulation protocol (TBS consisting of 4 short bursts at a frequency of 100 Hz with an interburst interval of 200 ms). Whole cell patch-clamp recordings on CA1 pyramidal neurons were performed to detect spontaneous excitatory postsynaptic currents (sEPSCs) events, AMPA/NMDA ratio and paired-pulse ratio (PPR), as previous published [49].

### Drugs

Amyloid  $\beta$ <sub>1–42</sub> and its scrambled form were purchased from GenScript (USA); Picrotoxin was purchased from Sigma-Aldrich (Italy); Minocycline hydrochloride was purchased from Abcam; Pexidartinib (PLX3397) was purchased from MedChemExpress (MCE; USA); 4',6-diamidino-2-phenylindole (DAPI) was purchased from Life Technologies, (Carlsbad, CA, USA), goat anti-Iba1 (AB5076) from Abcam, rat anti-CD68 (BRDMCA1957T) from Bio-Rad Laboratories S.r.l. (Italy); rabbit anti-vGLUT1 (135303) from Synaptic System (GmbH, Goettingen, Germany); mouse anti-vGLUT1 (MAB5502; clone 3C10.2, Merck-Millipore, Darmstadt, Germany) from Merck Millipore; mouse anti-beta Amyloid (mabn254; MOAB-2, clone 6c3) from Merck (Darmstadt, Germany).

**Immunofluorescence staining.** After recovery from cutting procedure for 1 h at room temperature (24  $\pm$  2  $^{\circ}$ C) and pharmacological treatments, parasagittal hippocampal slices (250  $\mu$ m thick) were fixed by immersion in 10 mL of 4% PFA (paraformaldehyde) overnight (ON) at 4  $^{\circ}$ C and washed with 0.1 M phosphate buffer saline (PBS). Thick brain slices for all immunohistochemistry were collected in separate wells of a 24 wells plate (Nunc) and processed as free-floating sections.

Slices were washed with PBS and the appropriate Alexa-conjugated secondary antibody was incubated in PBS + 0.1% Triton for 3 h at RT in the dark.

For single labeling we used the anti-Iba1 (1:1000) primary antibody and the secondary anti-goat Alexa-555 antibody (1:200); the anti-CD68 (1:100) primary antibody and the secondary anti-rabbit Alexa-488 (1:600) antibody; the anti-soluble amyloid MOAB-2 (1:100) primary antibody and the secondary anti-mouse Alexa-546 (1:1000) antibody.

For the double immunofluorescent staining, a mixture of primary antibodies against MOAB-2 (1:100)/anti-vGlut1 (1:100) followed by a combination of secondary anti-mouse Alexa-546 (1:1000)/anti-rabbit Alexa-488 (1:1000) antibodies.

For triple labeling, a mixture of primary antibodies against MOAB-2(1:100)/anti-Iba1(1:1000)/anti-CD68 (1:100) followed by a combination of secondary anti-mouse Alexa-546 (1:1000)/anti-Goat Alexa 647 (1:600)/anti-rat Alexa-488 (1:1000)/ antibodies; or a mixture of primary antibodies anti-vGlut1(1:100)/anti-Iba1(1:1000)/anti-CD68 (1:100)/followed by a combination of secondary anti-mouse Alexa-546(1:600)/ anti-goat Alexa-647 (1:1000)/anti-rat Alexa-488 (1:1000) antibodies.

Slices were stretched in anatomical order onto SuperFrost Plus glass slides and then cover-slipped using #1 thickness (0.13–0.16 mm) thickness glass coverslips (Fisher) and ProLong Diamond mounting medium with antifading (P36931; Life Technologies, Carlsbad, CA, USA). An UV diode laser operating at 405 nm, an Argon laser at 488 nm, and a HeNe lasers at 543 and 633 nm were used as excitation sources.

### Microglia morphological analysis

**Image acquisition.** Slice imaging was performed with a laser-scanning confocal microscope (Olympus FV1200) using 20 $\times$  air, 40 $\times$  (NA = 1.25) and 60 $\times$  oil immersion lenses at 1024  $\times$  1024 pixels per frame, 12 frames per stack at 0.29 mm interval (pinhole 1.0). Four non overlapping field of view (FOV) of the CA1 (including the SO, SP, SR) from each section were acquired.

Images were acquired with FV10-ASW software (Version 4.2, Olympus) and the Fiji build of ImageJ (RRID:SCR\_002285) software analysis was used to generate maximum intensity projections of each image for further analysis

**Image processing for quantification: Iba1 analysis.** The number of Iba1 positive microglial cells was counted by semi-automated analysis. Images acquired by 40 $\times$  oil Immersion objective were converted into 8 bit Images (gray levels), thresholded to include all microglial ramifications, and binarized.

**CD68 analysis.** The number of CD68 positive phagosomes was counted in images acquired by 60× immersion oil objective (1024×1024 pixels per frame).

**Colocalization analysis.** The triple immunofluorescence stainings of Iba1/CD68/amyloid and Iba1/CD68/vGlut1 were performed to study amyloid load and glutamatergic synapses pruning by microglial cells in the different experimental conditions and subsequently used for the colocalization analysis of the following combinations of markers: amyloid/Iba1, amyloid/CD68, vGlut1/Iba1 and vGlut1/CD68.

## Statistics

**Electrophysiology.** Data were expressed as mean ± SEM. Statistical comparisons of data obtained from electrophysiological experiments were performed using the Student's t-test (paired or unpaired data) or with one-way ANOVA followed by Bonferroni's post-hoc test. Statistical significance was set at  $p < 0.05$ .

In LTP experiments significance was evaluated between 50–60 min following delivery of conditioning trains. Changes in amplitude or inter-event interval of the spontaneous events were compared according to their median values, using the Student's t-test.

For all statistical comparisons, the  $n$  used was the number of slices or neurons.

**Imaging analysis.** All measurements values were averaged for each section for a total number of brain slices  $n = 5$  per experimental group and expressed as percentage of control (vehicle). The statistical analyses and the graphs were generated using Statview (Statview-SAS, Cary, NC, USA) and the data were reported in the graphs as mean ± SEM. ANOVA followed by the Tukey–Kramer post hoc or Student's t-test for group comparisons, depending on the number of variables and groups, were used to analyze the data. A  $p \leq 0.05$  was considered statistically significant.

## RESULTS

### CSF1R inhibition by PLX3397 or minocycline reverses A $\beta$ -mediated LTP impairment

As previously reported, application of soluble A $\beta_{1-42}$  impairs LTP at CA1 hippocampal synapses [50]. The treatment of slices for 30 min with 200 nM of A $\beta_{1-42}$  was able to inhibit LTP compared to slices treated with A $\beta_{scrambled}$  (A $\beta_{scrambled}$  1.5 ± 0.1 vs. A $\beta_{1-42}$  1.2 ± 0.1  $p < 0.001$ ; Fig. 1A) in which the magnitude of LTP was comparable to vehicle treated slices (vehicle 1.5 ± 0.1 vs. A $\beta_{scrambled}$  1.5 ± 0.1  $p > 0.05$ ; Fig. S1).

Minocycline is a tetracycline that also shows inhibitory activity on microglia activation [51]. The treatment of slices with minocycline prevented the significant reduction of LTP magnitude induced by A $\beta_{1-42}$  (A $\beta_{1-42}$ +minocycline 1.4 ± 0.1 vs. A $\beta_{1-42}$  1.2 ± 0.1  $p < 0.001$ ; Fig. 1B) that was comparable to LTP induced in slices treated with A $\beta_{scrambled}$ +minocycline (A $\beta_{1-42}$ +minocycline: 1.4 ± 0.1 vs. A $\beta_{scrambled}$ +minocycline: 1.4 ± 0.1  $p > 0.05$ ; Fig. 1B).

Since minocycline is a non-specific modulator of microglia response, we then used Pexidartinib (PLX), which is an orally bioavailable selective CSF1R tyrosine kinase inhibitor.

Here we show that hippocampal slices incubated with A $\beta_{1-42}$  + PLX showed a restoration of LTP compared to the A $\beta_{1-42}$  alone (A $\beta_{1-42}$  1.2 ± 0.1 vs. A $\beta_{1-42}$  + PLX 1.5 ± 0.1  $p < 0.001$ ; Fig. 1C) that was comparable to LTP induced in slices treated with A $\beta_{scrambled}$  + PLX (A $\beta_{1-42}$  + PLX 1.5 ± 0.1 vs. A $\beta_{scrambled}$  + PLX 1.5 ± 0.1  $p > 0.05$ ; Fig. 1C).

Altogether, these data demonstrate the involvement of microglia in the A $\beta_{1-42}$ -mediated alteration of hippocampal LTP.

### PLX3397 reverses A $\beta$ -driven excitatory neurotransmission alteration

As described previously [50], perfusion of A $\beta_{1-42}$  (500 nM, 10 min) induces a significant increase in PPR (vehicle 1.9 ± 0.1 vs. +A $\beta$  2.7 ± 0.3  $p < 0.01$ ; Fig. 2A) compared to baseline, which reflects a transient decrease in the probability of vesicular release. Application of PLX (10  $\mu$ M, 30 min) before and during A $\beta_{1-42}$  perfusion

(500 nM, 10 min) normalized the PPR to the baseline level, while PLX alone did not affect the PPR (vehicle + A $\beta_{1-42}$  2.7 ± 0.3 vs. PLX + A $\beta_{1-42}$  1.6 ± 0.1  $p < 0.01$ ; PLX 2.0 ± 0.3 vs. PLX + A $\beta_{scrambled}$  1.9 ± 0.3  $p > 0.05$ ; Fig. 2A).

Then we have investigated the excitatory neurotransmission analyzing the AMPA/NMDA ratio, a measure of postsynaptic changes in synaptic strength, and the amplitude and frequency of spontaneous excitatory post synaptic currents (sEPSCs) which reflect changes in glutamatergic neurotransmission efficacy. It is known that A $\beta_{1-42}$  application in brain slices affects the synaptic distribution of both receptor subtypes [52]. In our model, A $\beta_{1-42}$  (500 nM, 10 min) induced an increase in the AMPA/NMDA ratio which was prevented by application of PLX before (10  $\mu$ M, 30 min) and during A $\beta_{1-42}$  perfusion (vehicle 1.4 ± 0.2 vs. vehicle + A $\beta_{1-42}$  2.0 ± 0.2  $p < 0.01$ ; PLX 1.6 ± 0.1 vs. PLX + A $\beta_{1-42}$  1.6 ± 0.1  $p < 0.01$ ; Fig. 2B), suggesting that blocking the CSF1 receptor affects synaptic changes induced by A $\beta_{1-42}$  (PLX 1.6 ± 0.1 vs. PLX + A $\beta_{scrambled}$  1.6 ± 0.2  $p > 0.05$ ; Fig. 2B;  $n = 5$ ).

Also, we found that in same experimental conditions application of PLX with A $\beta_{1-42}$  prevented the sEPSC amplitude and frequency changes induced by A $\beta_{1-42}$  alone (amplitude: vehicle 100.0 ± 9.4 vs. vehicle + A $\beta_{1-42}$  83.2 ± 5.7  $p < 0.05$ ; PLX 100.0 ± 6.2 vs. PLX + A $\beta_{1-42}$  99.1 ± 5.7,  $p > 0.05$ ; frequency: vehicle 100.0 ± 14.0 vs. vehicle + A $\beta_{1-42}$  54.5 ± 5.8  $p > 0.05$ ; PLX 100.0 ± 7.7 vs. PLX + A $\beta$  100.1 ± 8  $p > 0.05$ ; Fig. 2C), while the treatment with PLX and A $\beta_{scrambled}$  did not induce any change (amplitude: PLX 100.0 ± 4.6 vs. PLX + A $\beta_{scrambled}$  91.7 ± 6.5,  $p > 0.05$ ; frequency: PLX 100.0 ± 3 vs. PLX + A $\beta_{scrambled}$  91.5 ± 18.9; Fig. 2C).

Altogether, these data demonstrate the involvement of microglia in the A $\beta_{1-42}$ -mediated excitatory neurotransmission impairments.

### A microglial morphological switch toward the phagocytic phenotype is promoted by PLX3397 in hippocampal slices with A $\beta_{1-42}$

The Fig. 3B shows that the number microglia per field of view (FOV), as identified by Iba1+ (red) staining, were counted and found to be comparable in the different experimental conditions ( $p = 0.8079$ ; vehicle 100.6 ± 4.9; A $\beta_{1-42}$  104.2 ± 17.2; A $\beta_{1-42}$  + PLX 115.1 ± 6.4; A $\beta_{scrambled}$  107.3 ± 10.3). The Iba1 positive area per cell was evaluated as a measure of the average microglial size (Fig. 3C), and was found to be significantly increased upon PLX treatment (A $\beta_{1-42}$  + PLX) compared to A $\beta_{1-42}$  (\*\* $p < 0.01$ ) and A $\beta_{scrambled}$  (\* $p < 0.05$ ) groups ( $p = 0.0016$ ; vehicle 125.0 ± 11.6; A $\beta_{1-42}$  89.6 ± 7.6; A $\beta_{1-42}$  + PLX 153.9 ± 12.7; A $\beta_{scrambled}$  102.6 ± 14.4). Also, the microglial perimeter was investigated (Fig. 3D) and observed to significantly augment in A $\beta_{1-42}$  + PLX compared with vehicle (\* $p < 0.05$ ), A $\beta_{1-42}$  (\*\* $p < 0.01$ ), and A $\beta_{scrambled}$  (\*\* $p < 0.01$ ) groups ( $n = 10$ /group;  $p = 0.0003$ ; vehicle 100.0 ± 8.8; A $\beta_{1-42}$  76.5 ± 6.5; A $\beta_{1-42}$  + PLX 130.1 ± 8.6; A $\beta_{scrambled}$  79.1 ± 11.3). In line with an increased CI (\* $p < 0.05$ ), the amoeboid-like morphology of microglia upon A $\beta_{1-42}$  exposure can be easily noted in the representative binary mask (Fig. 3E).

The enlarged microglial phenotype is the most evident in the A $\beta_{1-42}$  + PLX group, with increased frequency of the phagocytic pocket, a subcellular structure dedicated to the digestion of phagocytosed materials (indicated by the blue arrow). In the A $\beta_{1-42}$  and A $\beta_{scrambled}$  group microglia has sometimes a bushy appearance. To specifically highlight the presence of amoeboid microglia we measured the circularity index (CI) (Fig. 3F). The CI is commonly used as a measure of microglial activation/function, and it falls in a range from 0 to 1, with 0 corresponding to a polyhedral shape and 1 to a perfectly round object. Of note, A $\beta_{1-42}$  induced a statistically higher CI value compared to vehicle (\*,  $p < 0.05$ ), as reported in the graph of Fig. 3F ( $n = 30$ /group;  $p < 0.0001$ ; vehicle 0.3 ± 0.04; A $\beta_{1-42}$  0.5 ± 0.04; A $\beta_{1-42}$  + PLX 0.597 ± 0.02; A $\beta_{scrambled}$  0.327 ± 0.03). Noteworthy, the PLX

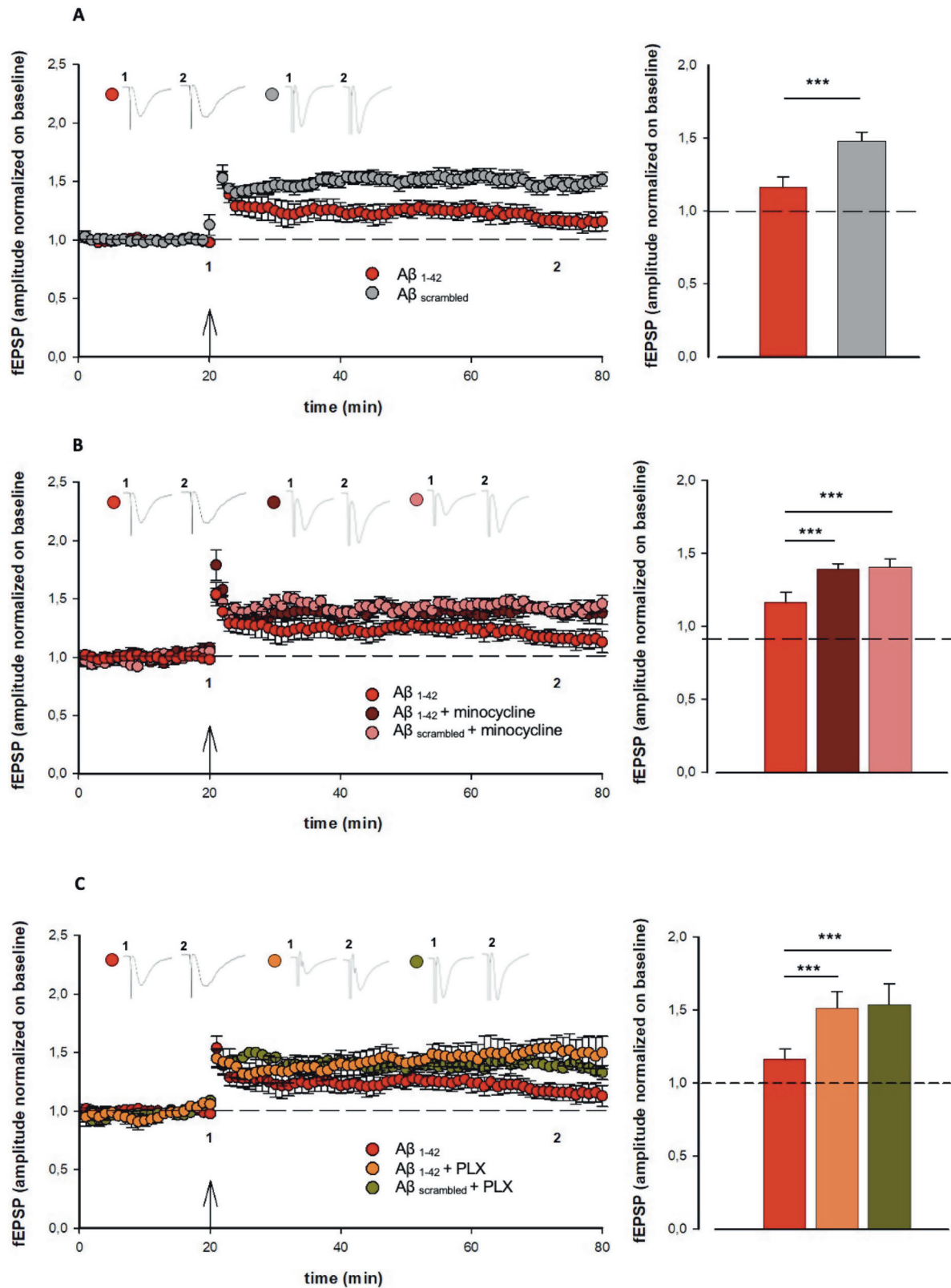


**Fig. 1** Minocycline and PLX3397 reverse  $A\beta$ -mediated LTP impairment. **A** On the left, superimposed pooled data showing LTP in slices treated with  $A\beta_{1-42}$  ( $n = 8$ ) or  $A\beta_{scrambled}$  ( $n = 8$ ). On top, representative traces for both conditions are shown. On the right, histograms illustrating the magnitude of LTP (% of baseline) in the two experimental conditions. **B** On the left, superimposed pooled data showing LTP in slices treated with  $A\beta_{1-42}$  ( $n = 8$ ),  $A\beta_{1-42} + \text{minocycline}$  ( $n = 8$ ) or  $A\beta_{scrambled} + \text{minocycline}$  ( $n = 6$ ). On top, representative traces for both conditions are shown. On the right, histograms illustrating the magnitude of LTP (% of baseline) in the different experimental conditions. **C** On the left, superimposed pooled data showing LTP in slices treated with  $A\beta_{1-42}$  ( $n = 8$ ),  $A\beta_{1-42} + \text{PLX}$  ( $n = 7$ ) or  $A\beta_{scrambled} + \text{PLX}$  ( $n = 7$ ). On top, representative traces for different experimental conditions are shown. On the right, histograms illustrating the magnitude of LTP (% of baseline) in the different experimental conditions. \*\*\* $p < 0.001$ .



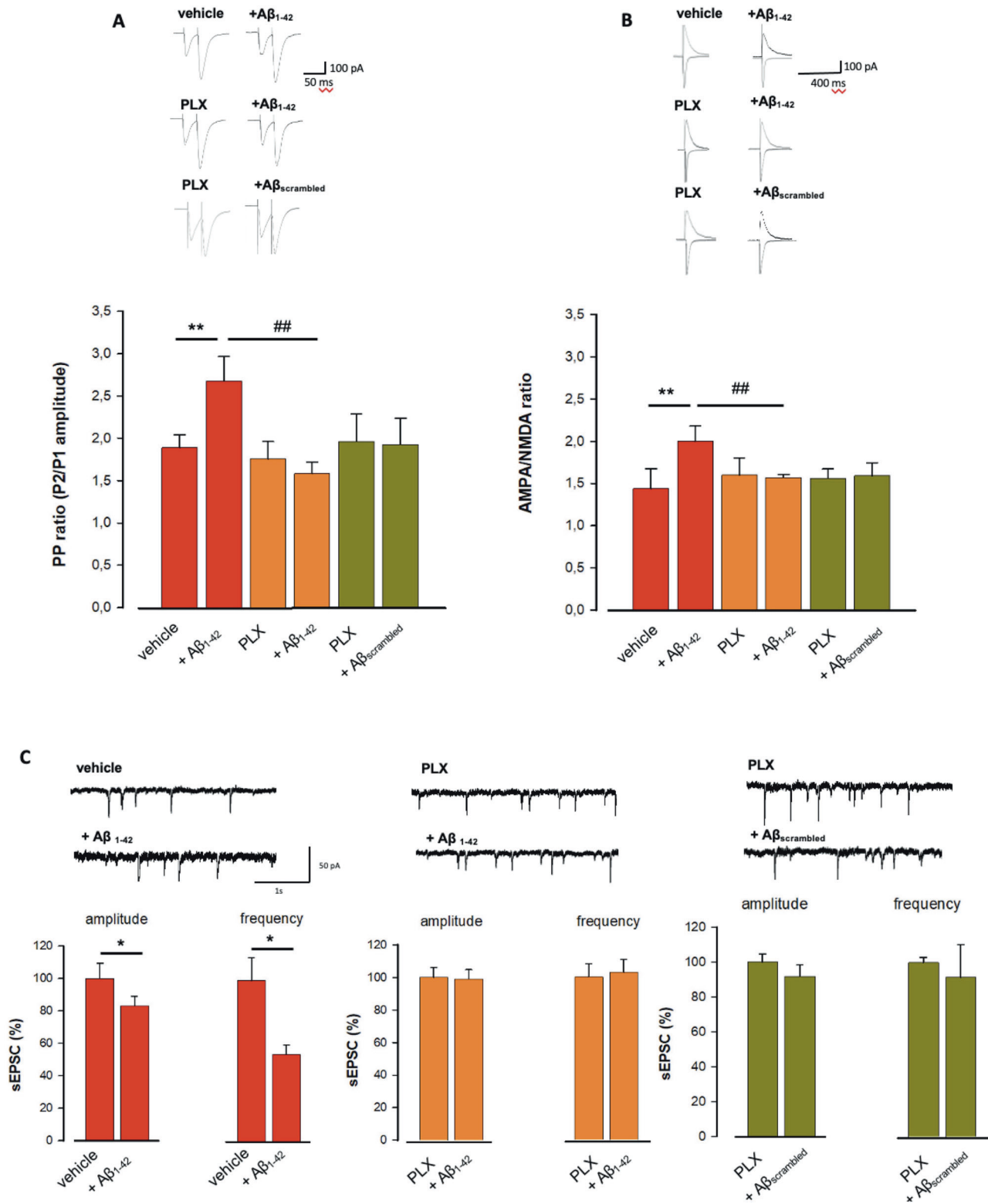


**Fig. 2** PLX3397 reverses excitatory neurotransmission alterations Aβ-mediated. **A** On top, representative traces from different experimental conditions are shown; on the right, histograms show change in PPR in different experimental conditions, vehicle+Aβ<sub>1-42</sub> (n=8), PLX + Aβ<sub>1-42</sub> (n=7), PLX+ Aβ<sub>scrambled</sub> (n=7). \*\*p<0.001 Aβ<sub>1-42</sub> vs. vehicle; ##p<0.001 Aβ<sub>1-42</sub> vs. PLX + Aβ<sub>1-42</sub>. **B** On top, representative traces in different experimental condition are shown. On the right, histograms show AMPA/NMDA ratio in different experimental conditions, vehicle+Aβ<sub>1-42</sub> (n=8), PLX + Aβ<sub>1-42</sub> (n=7), PLX + Aβ<sub>scrambled</sub> (n=7). \*\*p<0.001 Aβ<sub>1-42</sub> vs. vehicle; ##p<0.001 Aβ<sub>1-42</sub> vs. PLX + Aβ<sub>1-42</sub>. **C** On top representative traces from different experimental conditions are shown. The histograms show the effect of Aβ<sub>1-42</sub> on amplitude and frequency of sEPSC (as % of baseline) in different experimental conditions, vehicle + Aβ<sub>1-42</sub> (n=5), PLX + Aβ<sub>1-42</sub> (n=6), PLX + Aβ<sub>scrambled</sub> (n=5) \*p<0.05.

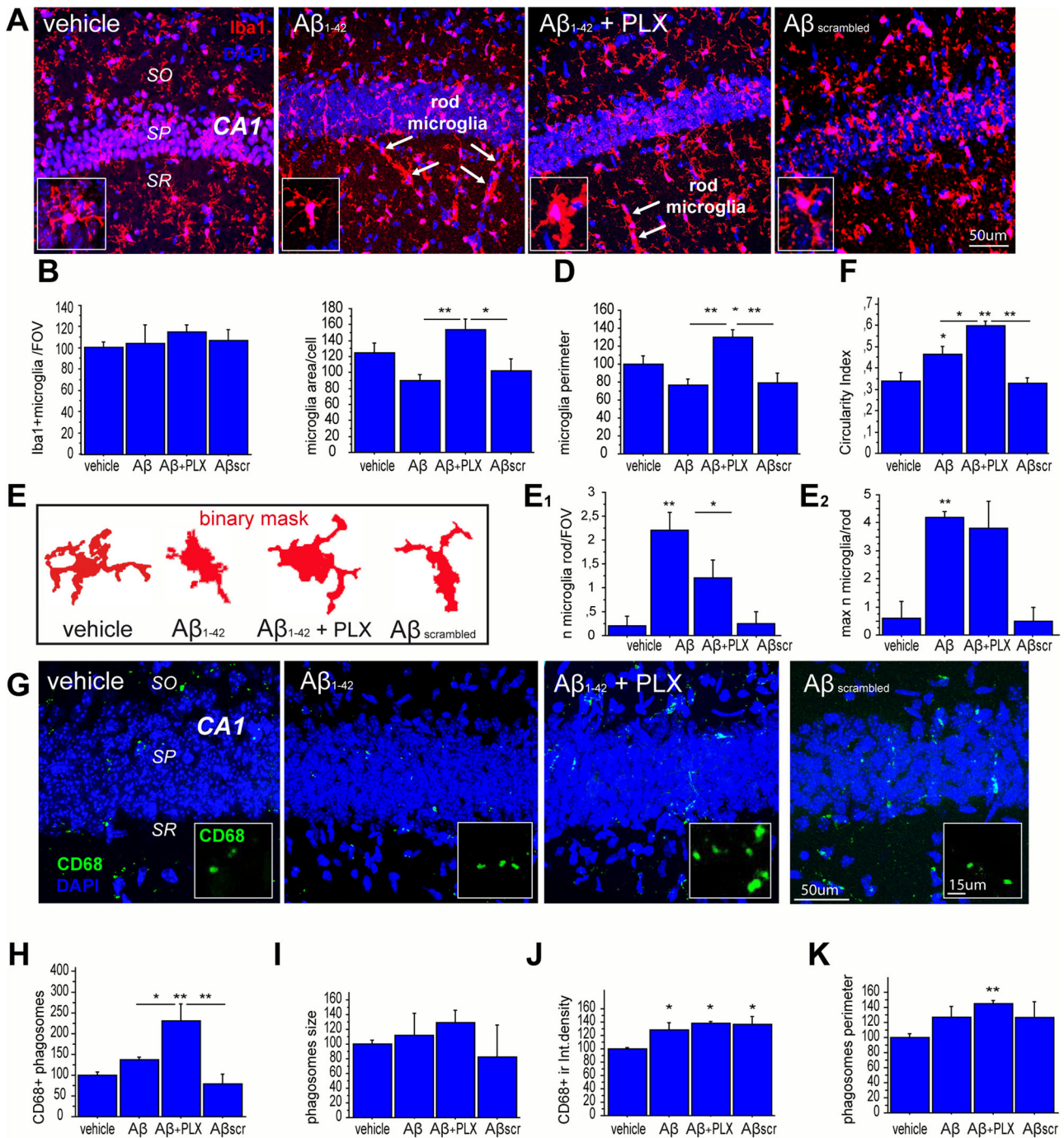


**Fig. 3 Morphological characterization of  $A\beta_{1-42}$  incubated hippocampal microglia with or without PLX3397 treatment.** **A** Representative immunofluorescence image of Iba1 positive (red) staining for microglia in the hippocampal CA1 region of vehicle,  $A\beta_{1-42}$ ,  $A\beta_{1-42} + PLX$  and  $A\beta_{scrambled}$  groups ( $n = 7/\text{group}$ ). **B** Numbers of Iba1+ microglia per field of view (FOV) were counted and no change was found in the different experimental conditions ( $p = 0.8079$ ). **C** The Iba1-positive area per cell was evaluated as a measure of the average microglial size, and found to be significantly increased upon PLX treatment ( $A\beta_{1-42} + PLX$ ) compared to  $A\beta_{1-42}$  (\*\* $p < 0.01$ ) and  $A\beta_{scrambled}$  (\* $p < 0.05$ ) groups ( $n = 10/\text{group}$ ). **D** Perimeter of Iba1-positive microglial cell was found significantly augmented in  $A\beta_{1-42} + PLX$  compared with vehicle (\* $p < 0.05$ ),  $A\beta_{1-42}$  (\*\* $p < 0.01$ ), and  $A\beta_{scrambled}$  (\*\* $p < 0.01$ ) groups. **E** The representative binary mask of microglial cells showing the morphological profile of microglia in the different experimental conditions. **F** The circularity index (CI) was calculated to verify the state of microglial activation based on its morphology. Treatment with PLX significantly increased the CI compared with vehicle (\*\* $p < 0.01$ ),  $A\beta_{1-42}$  (\* $p < 0.05$ ) and  $A\beta_{scrambled}$  (\*\* $p < 0.01$ ) groups. Also,  $A\beta_{1-42}$  induced a statistically significant upward trend of CI compared with vehicle (\* $p < 0.05$ ) group. **G** Representative immunofluorescent images showing immunofluorescent labeling for CD68 positive phagosomes (green) in the hippocampal CA1 region. High magnification of CD68 positive phagosome is shown in the insets. **H** The numbers of phagosomes are significantly increased upon PLX treatment ( $A\beta_{1-42} + PLX$ ) compared to vehicle (\*\* $p < 0.01$ ),  $A\beta_{1-42}$  (\* $p < 0.05$ ) and  $A\beta_{scrambled}$  (\*\* $p < 0.01$ ) groups ( $n = 4/\text{group}$ ). **I**  $n = 4/\text{group}$ ; **J**, **K** The perimeter of CD68+ phagosomes was also measured and it was found to increase in  $A\beta_{1-42} + PLX$  compared with vehicle (\*\* $p < 0.01$ ) group. DAPI (blue) was used to counterstain nuclei. CA1 Cornu Ammonis 1, SO stratum oriens, SP stratum pyramidale, SR stratum radiatum. White arrows: rod-like microglia. Scale bars: A, 50  $\mu\text{m}$ ; G, 50  $\mu\text{m}$ ; islet in G, 15  $\mu\text{m}$ . Graph bars indicate mean  $\pm$  SEM.



treatment of A $\beta_{1-42}$  exposed slices (A $\beta_{1-42}$  + PLX) was able to increase the microglia CI against the vehicle group also to a higher extent than A $\beta_{1-42}$  alone (\*\* $p < 0.01$ ), being significantly augmented also against the A $\beta_{1-42}$  alone (\*\* $p < 0.05$ ). A significant difference was also observed against the A $\beta_{\text{scrambled}}$  (\*\* $p < 0.01$ ) group. Also, the effect of PLX treatment alone on all the microglia-related parameters above reported was assessed (Fig. S5) and compared both to the vehicle and to the A $\beta_{1-42}$  + PLX groups: the

number of microglial cells per FOV ( $n = 30/\text{group}$ ;  $p = 0.769$ ; vehicle  $100.0 \pm 2.6$ ; PLX  $90.5 \pm 1.0$ ; A $\beta_{1-42}$  + PLX  $97.1 \pm 4.5$ ); the mean cell area ( $n = 30/\text{group}$ ;  $p = 0.9037$ ; vehicle  $100.0 \pm 9.9$ ; PLX  $107.9 \pm 55.0$ ; A $\beta_{1-42}$  + PLX  $122.9 \pm 29.3$ ); the microglial cell perimeter ( $n = 30/\text{group}$ ;  $p = 0.24$ ; vehicle  $100.0 \pm 6.5$ ; PLX  $210.0 \pm 70.7$ ; A $\beta_{1-42}$  + PLX  $121.5 \pm 20.9$ ); and the Circulatory Index ( $n = 30/\text{group}$ ;  $p < 0.0001$ ; vehicle  $0.30 \pm 0.01$ ; PLX  $0.36 \pm 0.01$ ; A $\beta_{1-42}$  + PLX  $0.55 \pm 0.03$ ). Of note, although a tendency was found

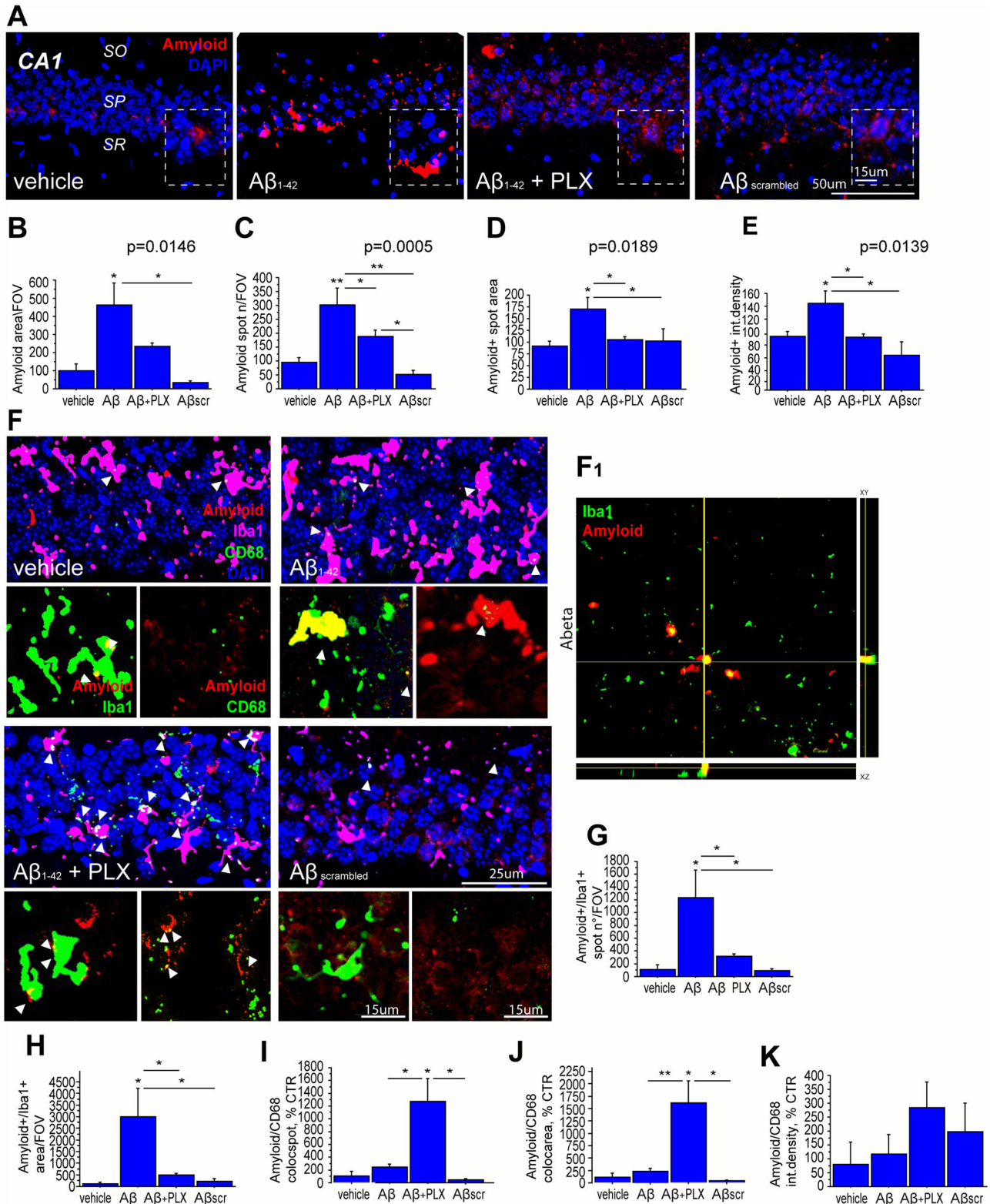


**Fig. 4 Acute PLX3397 treatment alleviates A $\beta$ <sub>1–42</sub> pathology in hippocampal slices.** **A** Representative amyloid immunofluorescence staining (red) by the MOAB2 antibody in the hippocampal CA1. High magnifications of amyloid staining are shown in the insets. **B** The total amyloid area per FOV was measured and found to be significantly increased in A $\beta$ <sub>1–42</sub> group compared to vehicle (\**p* < 0.05) and A $\beta$ <sub>scrambled</sub> (\**p* < 0.05) groups (*n* > 3/group). **C** The number of amyloid positive spots regardless of their size are statistically increased in A $\beta$ <sub>1–42</sub> (\**p* < 0.05), A $\beta$ <sub>1–42</sub> + PLX (\**p* < 0.05) and A $\beta$ <sub>scrambled</sub> (\**p* < 0.05) groups compared to vehicle (*n* = 5/group). **D** The area of the amyloid positive spots was found elevated in A $\beta$ <sub>1–42</sub> group compared with vehicle (\**p* < 0.05), PLX + A $\beta$ <sub>1–42</sub> (\**p* < 0.05) and A $\beta$ <sub>scrambled</sub> (*n* > 3; \**p* < 0.05) groups. **E** Amyloid staining intensity as measured by integrated density is significantly increased in the A $\beta$ <sub>1–42</sub> group compared with vehicle (\**p* < 0.05), PLX + A $\beta$ <sub>1–42</sub> (\**p* < 0.05) and A $\beta$ <sub>scrambled</sub> (\**p* < 0.05) groups (*n* > 4/group). **F** Analysis of amyloid distribution in microglial cells by triple immunofluorescence staining (upper image) for Iba1 (magenta), CD68 (green) and A $\beta$  (red) in the four experimental groups (vehicle, A $\beta$ <sub>1–42</sub>, A $\beta$ <sub>1–42</sub> + PLX and A $\beta$ <sub>scrambled</sub>). Composite images of amyloid (red) and Iba1 (green) immunofluorescence channels or of amyloid (red) and CD68 (green) immunofluorescence channels are shown in the high magnification images (images below) for each experimental group. Arrowheads point to area of markers colocalization. **F<sub>1</sub>** Orthogonal side views along the XZ and XY planes from the confocal z-stack of the amyloid/Iba1 confocal staining (Fiji, ImageJ, NIH, USA). **G** The numbers of the amyloid/Iba1 colocalized spots is significantly increased by A $\beta$ <sub>1–42</sub> compared to vehicle (\**p* < 0.05), A $\beta$ <sub>1–42</sub> + PLX (\**p* < 0.05) and A $\beta$ <sub>scrambled</sub> (\**p* < 0.05) groups (*n* > 3/group). **H** The area of the amyloid/Iba1 colocalized spots is significantly augmented in A $\beta$ <sub>1–42</sub> group compared to vehicle (\**p* < 0.05), PLX + A $\beta$ <sub>1–42</sub> (\**p* < 0.05) and A $\beta$ <sub>scrambled</sub> (\**p* < 0.05) groups (*n* > 3/group). **I** The numbers of the amyloid/CD68 colocalized spots significantly increased by PLX treatment compared to vehicle (\**p* < 0.05), A $\beta$ <sub>1–42</sub> (\**p* < 0.05) and A $\beta$ <sub>scrambled</sub> (\**p* < 0.05) groups (*n* > 3/group). **J** The area of the amyloid/CD68 colocalized spots is significantly increased by PLX treatment compared to vehicle (\**p* < 0.05), A $\beta$ <sub>1–42</sub> (\*\**p* < 0.01) and A $\beta$ <sub>scrambled</sub> (\**p* < 0.05) groups (*n* > 3/group). **K** Intensity of amyloid/CD68 colocalization is comparable to vehicle in all the experimental groups analyzed (*n* > 3. DAPI (blue) was used to counterstain nuclei. Graph bars indicate mean  $\pm$  SEM. Scale bars: **A**, 50  $\mu$ m; islet: 15  $\mu$ m; **F**, 25  $\mu$ m; islet: 15  $\mu$ m.

toward the increase of microglia perimeter and CI in the PLX group, this was not statistically significant, as compared to the vehicle or the A $\beta$ <sub>1–42</sub> + PLX groups; while a significant increase in the CI of the A $\beta$ <sub>1–42</sub> + PLX group both versus the vehicle and the PLX groups was confirmed (\*\**p* < 0.001).

The characterization of the microglial phenotype included the count and analysis of microglial phagosomes in the hippocampal CA1 region through the CD68 molecular marker (Fig. 3G–I, Fig. S2A). Phagosomes are specialized organelles implicated in phagocytosis and digestion of extracellular materials, including developmental and homeostatic neuronal pruning and amyloid clearance in AD [53, 54].

In line with previous findings, the numbers of phagosomes (Fig. 3H) are significantly increased upon PLX treatment of A $\beta$ <sub>1–42</sub> incubated brain slices (A $\beta$ <sub>1–42</sub> + PLX) compared to vehicle (\*\**p* < 0.01), A $\beta$ <sub>1–42</sub> (\**p* < 0.05) and A $\beta$ <sub>scrambled</sub> (\*\**p* < 0.01) groups (*p* = 0.0033; vehicle 100.0  $\pm$  7.5; A $\beta$ <sub>1–42</sub> 137.9  $\pm$  6.3; A $\beta$ <sub>1–42</sub> + PLX 231.7  $\pm$  40.7; A $\beta$ <sub>scrambled</sub> 78.4  $\pm$  23.1). Also, phagosome size (Fig. 3I) is increased by the PLX treatment as it can be appreciated by the CD68 positive spots perimeter (\*\**p* < 0.01) group (*p* = 0.1647; vehicle 100.0  $\pm$  5.4; A $\beta$ <sub>1–42</sub> 126.7  $\pm$  14.0; A $\beta$ <sub>1–42</sub> + PLX 145.3  $\pm$  3.8; A $\beta$ <sub>scrambled</sub> 126.3  $\pm$  21.1), and in the insets showing high magnification of CD68 staining (green). As for the PLX treatment alone Fig. S5, it was observed no significant difference in CD68 + phagosomes number (82.3  $\pm$  16.2), size (96.4  $\pm$  11.2) and perimeter (95.9  $\pm$  8.3), as compared to vehicle (respectively: 100.0  $\pm$  14.2; 100.0  $\pm$  8.2; 100.0  $\pm$  4.7), or A $\beta$ <sub>1–42</sub> + PLX (respectively: 75.0  $\pm$  25.3; 93.3  $\pm$  ), while a significant difference was found in the number of phagosomes/FOV, as compared to A $\beta$ <sub>1–42</sub> + PLX group, where an increase is observed (\**p* < 0.05; 218.7  $\pm$  41.6).

Interestingly enough, the appearance of rod-like microglia was noticed as sparse in the control group, as expected (vehicle; Fig. 3A), while it was found to be enhanced in the A $\beta$ <sub>1–42</sub> and also in the PLX + A $\beta$ <sub>1–42</sub> group, although to a minor extent (Fig. 3A, white arrows). Rod-like microglia is a chain of elongated microglial cells with narrowing of cells and soma and lacking planar processes preferentially observed in neuroinflammatory and AD-like conditions in the brain [55, 56].

The number of rod-like microglia and the higher number of microglial cells per rod were counted and compared (Fig. 1G, H). The measurements confirmed the qualitative observation, with an increase in rods number in the A $\beta$ <sub>1–42</sub> group (\*\**p* < 0.01; 2.2  $\pm$  0.4) and in A $\beta$ <sub>1–42</sub> + PLX (\**p* < 0.05; 1.2  $\pm$  0.4) as compared to vehicle (0.2  $\pm$  0.2) and A $\beta$ <sub>scrambled</sub> (0.25  $\pm$  0.25). Also, the maximum number of microglial cells observed per rod was significantly augmented in the A $\beta$ <sub>1–42</sub> group (\*\**p* < 0.01; 4.2  $\pm$  0.2) and in

A $\beta$ <sub>1–42</sub> + PLX (\**p* < 0.05; 3.8  $\pm$  1.0), as compared to vehicle (0.6  $\pm$  0.6) and A $\beta$ <sub>scrambled</sub> (0.5  $\pm$  0.5).

#### PLX3397 alleviates amyloid accumulation by promoting microglial phagocytosis of amyloid in A $\beta$ <sub>1–42</sub> exposed hippocampal slices

To ask for the effect on amyloid clearance of rapidly acquired phagocytic-like phenotype of microglia in A $\beta$ <sub>1–42</sub> + PLX hippocampal slices, we immunofluorescently labeled amyloid by using MOAB2. The MOAB2 antibody specifically recognizes extra and intracellular amyloid fragments, but not the entire APP molecule, at variance with the 6E10 clone [57]. The total MOAB2 immunolabelled area and staining intensity, as well as the number and area of soluble amyloid immunofluorescent staining, were measured and compared.

As expected, we observed an overall increase in the amyloid burden in the hippocampal CA1 region of the A $\beta$ <sub>1–42</sub> group as compared to both vehicle and A $\beta$ <sub>scrambled</sub>. This amyloid burden rise is found downregulated upon the PLX treatment of slices exposed to A $\beta$ <sub>1–42</sub>.

In details, the amyloid area (*p* = 0.0146; vehicle 100.0  $\pm$  38.4; A $\beta$ <sub>1–42</sub> 461.5  $\pm$  123.8; A $\beta$ <sub>1–42</sub> + PLX 233.6  $\pm$  19.8; A $\beta$ <sub>scrambled</sub> 35.3  $\pm$  10.0; Fig. 4B) was higher in the A $\beta$ <sub>1–42</sub> group compared to vehicle (\**p* < 0.05) and A $\beta$ <sub>scrambled</sub> (\**p* < 0.05) groups and also in the A $\beta$ <sub>1–42</sub> + PLX group the amyloid area is higher compared to vehicle (\**p* < 0.05). Noteworthy, the CA1 total amyloid area was comparable to vehicle upon PLX3397 treatment of A $\beta$ <sub>1–42</sub> incubated slices (A $\beta$ <sub>1–42</sub> + PLX group, *p* = 0.1066).

The number of amyloid positive spots regardless of their size are statistically increased in A $\beta$ <sub>1–42</sub> (\**p* < 0.05), and A $\beta$ <sub>scrambled</sub> (\**p* < 0.05) groups compared to vehicle (*p* = 0.0005 vehicle 93.9  $\pm$  17.0; A $\beta$ <sub>1–42</sub> 299.3  $\pm$  60.7; A $\beta$ <sub>1–42</sub> + PLX 187.8  $\pm$  22.0; A $\beta$ <sub>scrambled</sub> = 50.8  $\pm$  13.9). Interestingly, PLX treatment was also able to reduce the number of amyloid spots in the CA1 area of hippocampal slices incubated with A $\beta$ <sub>1–42</sub>, as compared to A $\beta$  group (Fig. 4C) (\**p* < 0.05). The size of amyloid spots, as measured by single spot area was also found to be elevated in A $\beta$ <sub>1–42</sub> group compared with vehicle (\**p* < 0.05), A $\beta$ <sub>1–42</sub> + PLX (\**p* < 0.05) and A $\beta$ <sub>scrambled</sub> (\**p* < 0.05) groups (*p* = 0.0189; vehicle 90.5  $\pm$  10.1; A $\beta$ <sub>1–42</sub> 169.9  $\pm$  24.8; A $\beta$ <sub>1–42</sub> + PLX 103.8  $\pm$  7.1; A $\beta$ <sub>scrambled</sub> 100.8  $\pm$  25.9; Fig. 4D).

The MOAB2 staining integrated density (corresponding to amyloid signal intensity) is upregulated in the A $\beta$ <sub>1–42</sub> group compared with vehicle (\**p* < 0.05), A $\beta$ <sub>1–42</sub> + PLX (\**p* < 0.05) and A $\beta$ <sub>scrambled</sub> (\**p* < 0.05) groups (*p* = 0.0139; vehicle 83.1  $\pm$  7.5; A $\beta$ <sub>1–42</sub> 134.1  $\pm$  19.4; A $\beta$ <sub>1–42</sub> + PLX 81.5  $\pm$  5.2; A $\beta$ <sub>scrambled</sub> 53.8  $\pm$  21.6; Fig. 4E).

Then, we tested the prediction that the amelioration of CA1 amyloid burden observed in the A $\beta$ <sub>1–42</sub> + PLX group may result



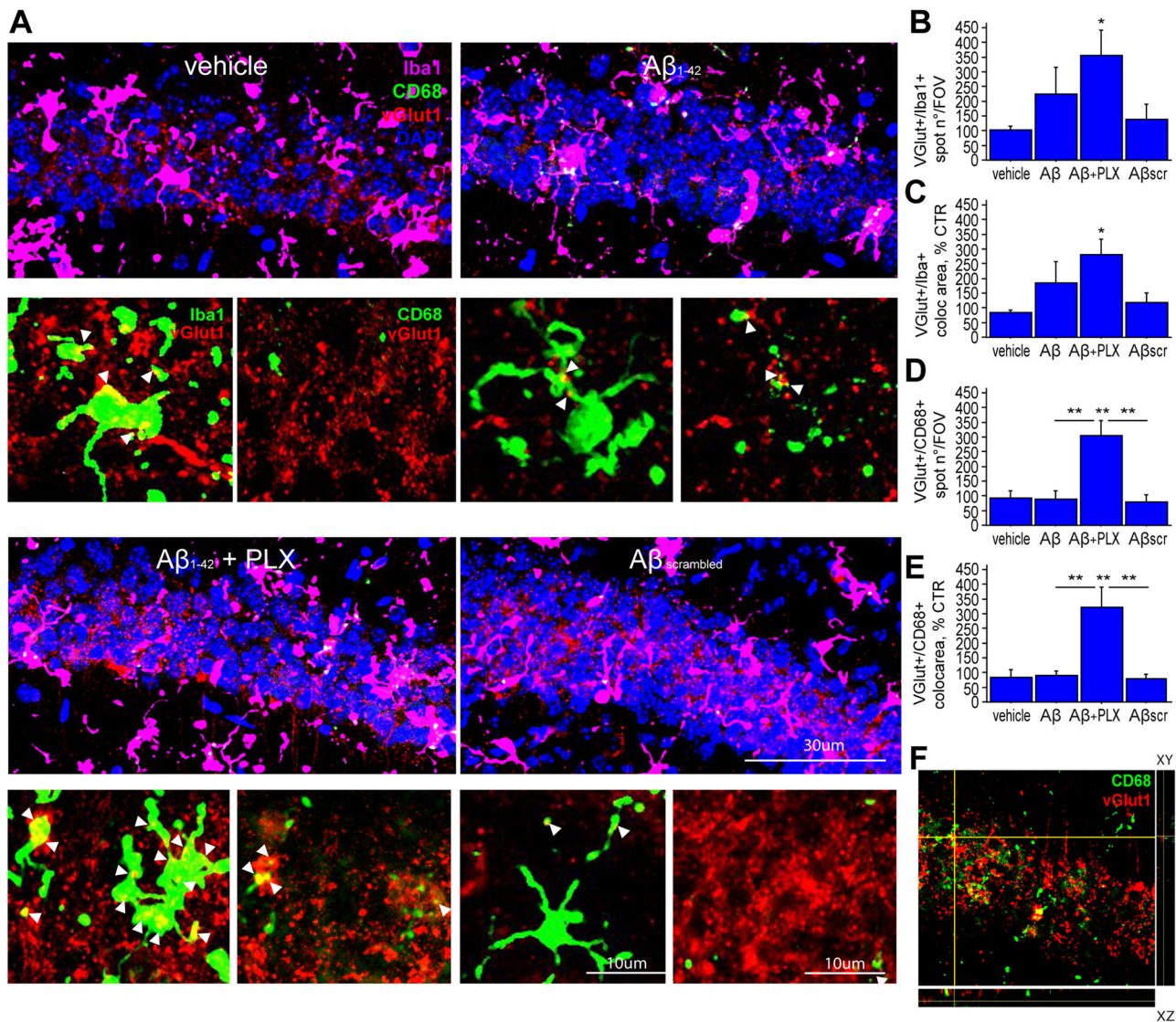


**Fig. 5** Acute PLX3397 treatment facilitates the microglial pruning of glutamatergic synapses. **A** Analysis of vGlut1 (red) engulfment in CD68 (green) phagocytic puncta of Iba1 positive (magenta) in the hippocampal CA1 region (upper image). DAPI (in blue) was used to counterstain nuclei. Composite images showing the vGlut1 (red) and Iba1 (green) or the vGlut1 (red) and CD68 (green) immunofluorescence channels are shown in the high magnification (images below). Arrowheads point to the colocalization of markers. **B** The number of vGlut1/Iba1 colocalization spots is significantly elevated upon PLX treatment compared to vehicle ( $*p < 0.05$ ) group. **C** Area of vGlut1/Iba1 colocalization spots is significantly increased in PLX + Aβ<sub>1-42</sub> group compared to vehicle ( $*p < 0.05$ ) group. **D** The number of vGlut1/CD68 colocalization spots is found increased in the Aβ+ group compared to vehicle ( $**p < 0.01$ ), Aβ<sub>1-42</sub> ( $**p < 0.01$ ) and Aβ<sub>scrambled</sub> ( $**p < 0.01$ ) groups ( $n > 4$ /group). **E** Area of vGlut1/CD68 colocalization spots is significantly increased in Aβ<sub>1-42</sub> + PLX group compared to vehicle ( $**p < 0.01$ ), Aβ ( $**p < 0.01$ ) and Aβ<sub>scrambled</sub> ( $**p < 0.01$ ) groups ( $n > 4$ /group). **F** The orthogonal side views (XZ, XY planes) from the confocal z-stack (Fiji, ImageJ, NIH, USA) of the vGlut1/CD68 double immunofluorescence staining confirm vGlut1 (red) staining within the CD68 positive phagosomal vesicles (green). Graph bars indicate mean ± SEM. Scale bars: upper image, 30 μm; images below, 10 μm.

from the observed morphological switch conferring increased phagocytic ability following PLX treatment. To ask this question, we studied the intracellular distribution of Aβ<sub>1-42</sub> in microglial cells by using the cytosolic Iba1 marker and the CD68 selective marker for phagocytic vacuoles in Iba1/CD68/amyloid triple immunolabelled hippocampal slices from all experimental groups (Fig. 4A and Fig. S3 for low magnification images). The cytosolic internalization and phagosome-dependent amyloid clearance signals were investigated, respectively by Iba1/amyloid and CD68/amyloid co-localization quantitative analysis. The Iba1/amyloid total colocalization area and spot number (Fig. 4G) are both augmented after Aβ<sub>1-42</sub> incubation of slices. In particular, the numbers of the amyloid/Iba1 colocalized spots is significantly increased by Aβ<sub>1-42</sub> compared to vehicle ( $*p < 0.05$ ), Aβ<sub>1-42</sub> + PLX

( $*p < 0.05$ ) and Aβ<sub>scrambled</sub> ( $*p < 0.05$ ) groups ( $p = 0.0169$ ; vehicle  $100.0 \pm 74.4$ ; Aβ<sub>1-42</sub>  $1227.3 \pm 428.8$ ; Aβ<sub>1-42</sub> + PLX  $305.5 \pm 46.0$ ; Aβ<sub>scrambled</sub>  $81.8 \pm 27.3$ ). Further, the area of the amyloid/Iba1 colocalized spots is significantly augmented in Aβ<sub>1-42</sub> group compared to vehicle ( $*p < 0.05$ ), Aβ<sub>1-42</sub> + PLX ( $*p < 0.05$ ) and Aβ<sub>scrambled</sub> ( $*p < 0.05$ ) groups ( $p = 0.0301$ ; vehicle  $100.0 \pm 71.9$ ; Aβ<sub>1-42</sub>  $297.4 \pm 1213.1$ ; Aβ<sub>1-42</sub> + PLX  $491.4 \pm 67.0$ ; Aβ<sub>scrambled</sub>  $221.9 \pm 99.5$ ; Fig. 4H). Notably, soluble amyloid accumulated in the brain slices incubated with Aβ<sub>1-42</sub> alone is endocytosed but not simply apposed to the outer surface of the microglial plasma membrane, as clearly visible in the XY, XZ orthogonal side views from the confocal z-stack of the Iba1/amyloid double staining, indicating that soluble amyloid (red) underneath the Iba1+ (green) microglial membrane (Fig. 5F<sub>1</sub>).



We then examined amyloid presence in the specialized CD68 positive vacuoles, by means of the following parameters: total colocalization spots number, spot area and colocalization signal intensity. Note that the vast majority of CD68+ phagosomes are within microglial cells in the hippocampal (Fig. 4F and Fig. S2C) and cortical area (Fig. S2B for low magnification images and islet

in B' for high magnification images) in our experimental conditions. We found that the number of CD68/amyloid spots increased upon PLX treatment compared to vehicle ( $*p < 0.05$ ),  $A\beta_{1-42}$  ( $*p < 0.05$ ) and  $A\beta_{scrambled}$  ( $*p < 0.05$ ) groups ( $p = 0.0065$ ; vehicle  $100.0 \pm 79.5$ ;  $A\beta_{1-42}$   $240.0 \pm 55.2$ ;  $A\beta_{1-42} + PLX$   $1294.3 \pm 363.0$ ;  $A\beta_{scrambled}$   $42.9 \pm 24.7$ ; Fig. 4I). Also, the area of

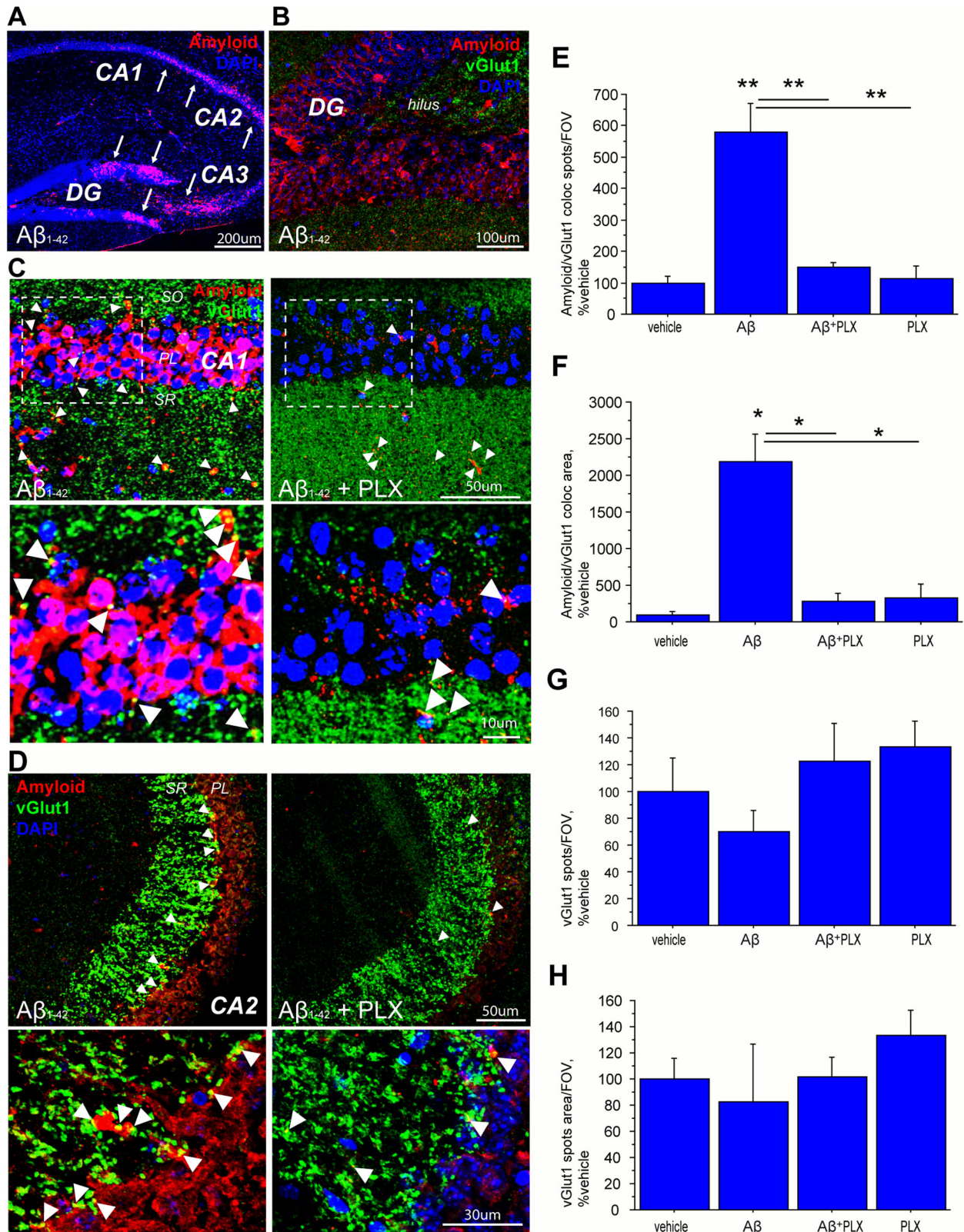


**Fig. 6 Acute PLX3397 treatment promotes clearing of A $\beta$ -loaded glutamatergic synapses in both the CA1 and CA2 hippocampal regions.** **A** Hippocampal areas where the amyloid staining (red) is more evident are indicated (white arrows) in slices incubated with A $\beta_{1-42}$ . **B** The vGlut1 (green) and amyloid (red) double immunofluorescent staining shows no clearly detectable amyloid at the vGlut1 glutamatergic terminals of A $\beta_{1-42}$  incubated hippocampal slices. **C** The vGlut1 (green) and amyloid (red) double immunofluorescent staining in the CA1 region of the hippocampus of the A $\beta_{1-42}$  and in the A $\beta_{1-42}$  + PLX groups is shown at low (upper image) and high (islet) magnifications. **D** The vGlut1 (green) and amyloid (red) double immunofluorescent staining in the CA2 region of the hippocampus of the A $\beta_{1-42}$  and in the A $\beta_{1-42}$  + PLX groups is shown at low and high (islet) magnifications. **E** The number of amyloid/vGlut1 colocalization spots is significantly augmented following amyloid incubation (A $\beta_{1-42}$  group,  $**p < 0.01$ ), as compared to both vehicle and PLX3397 alone (PLX) but normalizes to control level when amyloid is co-incubated with PLX3397 (A $\beta_{1-42}$  + PLX). **F** The area of amyloid/vGlut1 colocalization spots follows the same trend, with a significant increase in the A $\beta_{1-42}$  group, as compared to vehicle ( $*p < 0.05$ ), A $\beta_{1-42}$  + PLX ( $*p < 0.05$ ), and PLX ( $*p < 0.05$ ) groups. **G** The number and **H** the area of vGlut1-positive spots are comparable in all the experimental groups analyzed ( $p = 0.5834$  and  $p = 0.3427$ , respectively;  $n = 3$ /group). Arrowheads point to the vGlut1/amyloid colocalization puncta in both the cell body and dendritic layers of the CA1 and CA2. DAPI (blue) was used to counterstain nuclei. CA1-3 Cornu Ammonis 1-3, DG dentate gyrus. Scale bars: **A** 200  $\mu\text{m}$ ; **B** 100  $\mu\text{m}$ ; **C** 50  $\mu\text{m}$ ; islet, 10  $\mu\text{m}$ ; **D** 50  $\mu\text{m}$ ; islet, 30  $\mu\text{m}$ . SO *stratum oriens*, PL *stratum pyramidale*, SR *stratum radiatum*, CA2 Cornu Ammonis 2.

the amyloid/CD68 colocalized spots is significantly increased by PLX treatment compared to vehicle ( $*p < 0.05$ ), A $\beta_{1-42}$  ( $**p < 0.01$ ) and A $\beta_{\text{scrambled}}$  ( $*p < 0.05$ ) groups ( $p = 0.0050$ ; vehicle  $100.0 \pm 89.4$ ; A $\beta_{1-42}$   $234.5 \pm 62.7$ ; A $\beta_{1-42}$  + PLX  $1601.2 \pm 445.3$ ; A $\beta_{\text{scrambled}}$   $31.9 \pm 16.0$ ; Fig. 4J). Last, we found that the intensity of amyloid/CD68 colocalization is comparable to vehicle in all the experimental groups analyzed ( $p = 0.3770$ ; vehicle  $100.0 \pm 99.8$ ; A $\beta_{1-42}$   $145.8 \pm 89.6$ ; A $\beta_{1-42}$  + PLX  $357.4 \pm 116.4$ ; A $\beta_{\text{scrambled}}$   $246.8 \pm 130.3$ ; Fig. 4K).

#### Microglial pruning of glutamatergic synapses is facilitated by PLX3397 in A $\beta_{1-42}$ exposed hippocampal slices

Based on the increased phagocytotic activity of microglia under PLX treatment and the rescue effect of PLX on LTP alterations induced by amyloid exposure, we then asked whether glutamatergic pruning by microglia is modulated in our experimental conditions.

For this purpose, we triple immunolabelled hippocampal slices from all experimental groups with antibodies against Iba1, CD68 and amyloid (Fig. 5A and Fig. S4 for low magnification images) and studied the intracellular distribution of the glutamatergic marker vGlut1 in microglial cells by using the cytosolic Iba1 marker and in phagosomes through the CD68 marker. The cytosolic internalization and phagosome-dependent pruning of presynaptic glutamatergic terminals were quantified in Iba1/vGlut1 and CD68/vGlut1 composite images (Fig. 5A–E), in the CA1 region of interest, including the *stratum oriens*, *pyramidale* and *radiatum*, as reported in Fig. S3.

We found both the number ( $*p < 0.05$ ;  $p = 0.0769$ ; vehicle  $85.9 \pm 9.5$ ; A $\beta_{1-42}$   $189.7 \pm 76.5$ ; A $\beta_{1-42}$  + PLX  $300.0 \pm 73.1$ ; A $\beta_{\text{scrambled}}$   $116.7 \pm 43.4$ ; Fig. 5B) and the area ( $*p < 0.05$ ;  $p = 0.0417$ ; vehicle  $84.5 \pm 8.3$ ; A $\beta_{1-42}$   $189.9 \pm 74.1$ ; A $\beta_{1-42}$  + PLX  $290.3 \pm 53.2$ ; A $\beta_{\text{scrambled}}$   $121.2 \pm 33.2$ ; Fig. 5C) of vGlut1 (green)/Iba1 (red) colocalization spots significantly elevated upon PLX treatment compared to vehicle group. Further, we studied vGlut1 localization within phagosomes and observed that also the number of vGlut1/CD68 colocalization spots is found increased in the A $\beta_{1-42}$  + PLX group compared to vehicle ( $**p < 0.01$ ), A $\beta_{1-42}$  ( $**p < 0.01$ ) and A $\beta_{\text{scrambled}}$  ( $**p < 0.01$ ) groups ( $n > 4$ ;  $p = 0.0004$ ; vehicle  $100.0 \pm 26.5$ ; A $\beta_{1-42}$   $96.6 \pm 29.9$ ; A $\beta_{1-42}$  + PLX  $336.4 \pm 54.4$ ; A $\beta_{\text{scrambled}}$   $86.4 \pm 25.3$ ). Also, the vGlut1/CD68 colocalization area raised in A $\beta_{1-42}$  + PLX group compared to vehicle ( $**p < 0.01$ ), A $\beta_{1-42}$  ( $**p < 0.01$ ) and A $\beta_{\text{scrambled}}$  ( $**p < 0.01$ ) groups ( $n > 4$ ;  $p = 0.0010$ ; vehicle  $100.0 \pm 30.8$ ; A $\beta_{1-42}$   $107.1 \pm 17.1$ ; A $\beta_{1-42}$  + PLX  $391.7 \pm 83.4$ ; A $\beta_{\text{scrambled}}$   $92.6 \pm 19.6$ ). Of note, an effective pruning of glutamatergic spines is occurring, with vGlut1+ puncta actively phagocytosed, but not simply apposed or encapsulated by microglial cells, as noticeable in the orthogonal side views (XZ, XY planes) of the vGlut1/CD68 double immunofluorescence staining, showing vGlut1 (red) staining within CD68 positive phagosomal vesicles (green).

These data pinpoint a significant effect on microglial engulfment of glutamatergic terminals upon PLX treatment in the CA1 of A $\beta_{1-42}$  exposed hippocampal slice.

#### Rapid clearance of A $\beta$ -loaded glutamatergic synapses is observed upon CSF1R inhibition in the CA1-CA2 hippocampal regions, by preserving glutamatergic terminals

Last, we assessed whether PLX is able to clear engulfed glutamatergic terminals from intracellular amyloid, which is more evident in CA1, CA2, DG and hilus of hippocampal slices incubated with A $\beta_{1-42}$  (Fig. 6A). A double immunofluorescent staining against vGlut1 (green) and amyloid (red) was performed (Fig. 6B–D). The main hippocampal areas interested by vGlut1/Amyloid co-localization were the CA1 (Fig. 6C) and the CA2 (Fig. 6D), while it was almost undetectable in the DG (Fig. 6B). The images of Fig. 6C, D and respective high magnifications (insets) clearly show abundant colocalization of vGlut1 positive puncta with amyloid (yellow spots) in the A $\beta_{1-42}$  group, and very few co-localization spots in the A $\beta_{1-42}$  + PLX group. The extent of colocalization of soluble amyloid with vGlut1 + puncta in the CA1 was quantified and reported in the graphs (Fig. 6E, F). The number of amyloid/vGlut1 colocalization spots was found to be significantly higher in the brain slices incubated with amyloid (A $\beta_{1-42}$  group,  $**p < 0.01$ ;  $581.1 \pm 88.5$ ) as compared to control (vehicle;  $100.0 \pm 21.0$ ) but not when amyloid is co-incubated with PLX3397 (A $\beta_{1-42}$  + PLX;  $149.6 \pm 14.2$ ). No difference was found with PLX alone (PLX;  $112.6 \pm 39.8$ ). The same trend was observed by analyzing the area of amyloid/vGlut1 colocalization spots, with significant increase in the amyloid found in glutamatergic terminals of the A $\beta_{1-42}$  group ( $**p < 0.01$ ;  $2191.6 \pm 378.0$ ), as compared to vehicle ( $100.0 \pm 35.1$ ), to A $\beta_{1-42}$  + PLX ( $**p < 0.01$ ;  $278.03 \pm 111.1$ ) or to PLX alone (PLX;  $334.7 \pm 173.4$ ).

To investigate whether pruning of amyloid from glutamatergic terminals affects the extent of glutamatergic innervation in the CA1, we analyzed the vGlut1 staining pattern by measuring the number ( $p = 0.3427$ ) and area ( $p = 0.5834$ ) of vGlut1 + spots (Fig. 6G, H), but no significant differences were observed among the experimental groups.

Overall, we demonstrated that PLX treatment releases presynaptic glutamatergic neurons from the amyloid load without affecting overall glutamatergic staining, thus pinpointing PLX-driven clearance of amyloid burden in the CA1 and CA2 areas of the hippocampal slices incubated with A $\beta_{1-42}$ .

#### DISCUSSION

In this study we investigated how the pharmacological modulation of microglial function by direct application of the CSF1R selective inhibitor PLX3397, can reverse synaptic dysfunction in acute hippocampal slices exposed to A $\beta_{1-42}$ .

CSF1R inhibition by both minocycline and PLX3397 alleviated amyloid-mediated impairment of synaptic plasticity. Also, selective inhibitor PLX3397 prevents PPR, AMPA/NMDA ratio and sEPSC changes induced by A $\beta_{1-42}$ . On the same line, inactivating microglial CSF1R signaling by minocycline has been previously found to prevent soluble A $\beta$ -inhibited LTP in AD mice [58].



Then, we addressed microglial viability upon PLX3397 application and found no sign of microglial depletion; also, the number of Iba1-expressing cells is comparable in all the experimental conditions analyzed. Notably, depending on the dose, PLX can either deplete microglia or modify their function [38, 59]. The majority of CSF1R inhibitor trials showed a neuroprotective effect in chronic in vivo settings, which was mediated by reactive microglia repopulating the brain following microglial ablation [45, 60]. Nevertheless, a microglia-modulating dose of the CSF1R inhibitor PLX5622 [45] or of PLX3397 have also been shown to have neuromodulatory effect on hippocampal synaptic plasticity without affecting microglial survival [61, 62].

These data are in line with findings from haploinsufficient *csf1r*<sup>+/-</sup> mice, microglial-conditional *csf1r*<sup>-/-</sup> mice, hypomorphic *csf1r*<sup>FIRE-/-</sup> mice and in mice with rapid and low-grade CSF1R inhibition, showing microglial survival and a phenotypic switch toward a phagocytic status, without microglial proliferation and/or inflammation [44, 45, 47, 61].

Although controversial, a correlation between the morphology and function has been proposed for the microglial phenotypes (surveillant, phagocytic, amoeboid, rod-like) described so far [63], with e.g. phagocytic microglia appearing as less ramified and hypertrophic [64, 65].

To address this point, we characterized microglia morphology by confocal imaging analysis using specific markers of microglia (Iba1) and phagocytic organelles, called phagosomes (CD68). CSF1R inhibition by PLX3397 induced a rise in Iba1+ area and perimeter, as well as in the circularity index, characteristic of phagocytic microglia, including the phagocytic pocket, a preferred site for clearing of external material [66]. As a confirmation, we quantified CD68 staining and found an augmentation of the number, perimeter and CD68 staining intensity in phagosomes. Of note, the majority of phagosomes were found within Iba1+, ruling out phagocytic astrocytes' engagement [67], at least in our experimental conditions. When exposed to A $\beta$ <sub>1-42</sub> in absence of PLX3397, microglial cells display a less ramified phenotype with a higher circularity index as compared to control, as reported in neuroinflammatory microglia from mice i.c.v. injected with soluble A $\beta$ <sub>1-42</sub> [68] and in human AD microglia [69]. Inflammatory microglia in the human AD brain display increased level of CSF-1R and its ligands [70]. In turn, attenuated proliferation and inflammatory activation of microglia, resulting in neuroprotection was reported upon CSF1R pharmacological inhibition by JNJ-40346527 in P301S AD mice, by GW2580 in APP/PS1 mice and in MTPT mice, or by cSF1Rinh in EAE models [71-74]. Several studies agree that treatment with CSF-1R inhibitors decreases inflammation in AD, regardless of the extent of microglial depletion, or effects on A $\beta$  and Tau [75, 76]. As a further confirmation, hippocampal rod-like microglia [77] were prominent in the CA1 of A $\beta$ <sub>1-42</sub> slices and sparsely present in A $\beta$ <sub>1-42</sub>+PLX3397 (Fig. 1E<sub>1</sub>-E<sub>2</sub>). Rod microglia typically appear as a train of elongated cells typically found in the AD brain [78], lacking planar processes, and releasing pro-inflammatory cytokines, like TNF $\alpha$  and IL-1 [77]. It is well characterized that the accumulation of A $\beta$  during AD progression affects microglia through interaction with various receptors [19, 79, 80].

As a further step, we measured amyloid expression patterns. We found an augmented amyloid load in A $\beta$ <sub>1-42</sub> slices and a number of amyloid-related parameters, including total area, spots number, spot area, and integrated density were significantly augmented in A $\beta$ <sub>1-42</sub>, as inherently expected. Of note, the cytosol of microglial cells is notably engulfed by soluble amyloid in slices exposed to A $\beta$ <sub>1-42</sub> (Fig. 4F1), which is reported to be endocytosed via fluid phase micropinocytosis [81-83]. In line with phagocytic activity of microglia in A $\beta$ <sub>1-42</sub>+PLX3397 slices, a general lowering of soluble amyloid staining, and a significant reduction in the area covered by the amyloid staining occurred upon PLX3397 acute treatment, as compared to both A $\beta$ <sub>1-42</sub> and vehicle slices. Noteworthy, PLX3397 promoted amyloid clearance by phagosomes in A $\beta$ <sub>1-42</sub> incubated slices, as resulting by amyloid/CD68 colocalization analysis,

suggesting that hippocampal amyloid reduction takes place through phagosomal-dependent mechanisms in A $\beta$ <sub>1-42</sub> + PLX3397 slices.

AD microglia have a reduced ability to rapidly respond to brain challenges, such as neuronal clearance of toxic amyloid, interfering with pruning-dependent synaptic plasticity and accelerating the neurodegenerative process [20, 84]. To address this issue, we then investigated the clearance of vGlut1+ glutamatergic terminals by microglial cells exposed to A $\beta$ <sub>1-42</sub> alone or with CSF1R inhibition by PLX3397. Noteworthy, an improved clearance from intraneuronal soluble A $\beta$  in excitatory presynaptic terminals was accompanied by preservation of overall CA1 glutamatergic innervation, possibly resulting in the LTP recovery seen in A $\beta$ <sub>1-42</sub> + PLX3397 slices.

Although in the late phase AD inflammatory microglia affects neuronal plasticity and cognition by abnormal pruning [3, 75], in the early AD stage insufficient or ineffective synaptic pruning by dysfunctional microglia is a key driver of synaptic alterations, LTP deficits, and inadequate regenerative response [6]. In line with this, here we show that the A $\beta$ <sub>1-42</sub>-engulfed microglia pruning of glutamatergic synapses is comparable to untreated control slices as seen by Iba1/vGlu1 and CD68/vGlu1 colocalization patterns. As a result, vGlut1+ terminals are loaded with amyloid (Fig. 6C, D), thus resulting in the LTP and excitatory neurotransmission impairments observed in A $\beta$ <sub>1-42</sub> slices. Since some cortical and hippocampal neurons express CSF-1R [85], which has a role in intraneuronal amyloid accumulation in AD mice [36], a direct and microglia-independent effect of PLX3397 on intraneuronal amyloid cannot be excluded and deserves further explorations.

As a matter of fact, several limitations are present in preclinical model used to explore AD [86, 87]. Particularly, we have used acute exposure, of ex vivo preparation, to exogenous A $\beta$  oligomers that has been largely used to study alterations in neurotransmission and synaptic plasticity A $\beta$ -mediated underlying cognitive deficits characterizing this disorder. Similar results are described in several lines of transgenic mouse models of AD which have shown intrinsic limitation and experimental bias [86, 87]. In this light, can be supported that different non-clinical models represent a potential advantage for investigating disease-related targets and pathways.

Overall, our data support the idea that microglial phenotype/ states are conditions tuneable through precise timing and dosing of selective CSF1R inhibitors, further pinpointing low-grade and rapid CSF1R inhibition as a valid experimental tool for a deeper understanding of microglia behavior in preclinical studies as well as a promising target for the fine modulation of the microglial phenotype in clinical settings.

Microglia are implicated in brain homeostasis, neuroinflammation, and neurodegenerative diseases like AD, where microglial markers, like TREM2, help identify one of the 5 specific AD molecular subtypes, as recently reported by Tijms et al [88].

According to a recently growing body of literature, microglial imaging analysis by integrating microglial phenotype, metabolism, and functions [89-91]. Microglial cells undergo metabolic and morphological changes during spine pruning and amyloid clearance in both the normal and diseased brain, including AD [92-94], and CSF1/CSF1R system is a crucial signaling pathway in these events [95, 96].

The systemic CSF1R inhibition leading to long-term microglia-depletion is clinically unfeasible in AD patients for several reasons, including significant off-target side effects. Given its therapeutic potential in AD [36, 71], PD [97], MS [73], TBI [98], novel strategies based on the fine-tuning modulation of microglia metabolism and behavior are strongly expected as promising disease-modifying approaches for the treatment of neurodegenerative diseases.

#### DATA AVAILABILITY

The authors declare that all the data of this study are available from the corresponding author upon reasonable request.

## REFERENCES

- Piccioni G, Mango D, Saidi A, Corbo M, Nisticò R. Targeting microglia-synapse interactions in Alzheimer's disease. *Int J Mol Sci.* 2021;22:2342. <https://doi.org/10.3390/ijms22052342>.
- Yousefzadeh A, Piccioni G, Saidi A, Triaca V, Mango D, Nisticò R. Pharmacological targeting of microglia dynamics in Alzheimer's disease: Preclinical and clinical evidence. *Pharmacol Res.* 2022;184:106404.
- Prinz M, Jung S, Priller J. Microglia biology: one century of evolving concepts. *Cell.* 2019;179:292–311. <https://doi.org/10.1016/j.cell.2019.08.053>.
- Paolicelli RC, Bolasco G, Pagani F, Maggi L, Scianni M, Panzanelli P, et al. Synaptic pruning by microglia is necessary for normal brain development. *Science.* 2011;333:1456–8. <https://doi.org/10.1126/science.1202529>.
- Akiyoshi R, Wake H, Kato D, Horiuchi H, Ono R, Ikegami A, et al. Microglia enhance synapse activity to promote local network synchronization. *eNeuro.* 2018;5:ENEURO.0088–18.2018 <https://doi.org/10.1523/ENEURO.0088-18.2018>.
- Neumann H, Kotter MR, Franklin RM. Debris clearance by microglia: an essential link between degeneration and regeneration. *Brain.* 2008;132:288–95. <https://doi.org/10.1093/brain/awn109>.
- Miyamoto A, Wake H, Ishikawa AW, Eto K, Shibata K, Murakoshi H, et al. Microglia contact induces synapse formation in developing somatosensory cortex. *Nat Commun.* 2016;7:12540 <https://doi.org/10.1038/ncomms12540>.
- Schafer DP, Lehrman EK, Kautzman AG, Koyama R, Mardinly AR, Yamasaki R, et al. Microglia sculpt postnatal neural circuits in an activity and complement-dependent manner. *Neuron.* 2012;74:691–705. <https://doi.org/10.1016/j.neuron.2012.03.026>.
- Hickman SE, Kingery ND, Ohsumi TK, Borowsky ML, Wang L, Means TK, et al. The microglial sensome revealed by direct RNA sequencing. *Nat Neurosci.* 2013;16:1896–905. <https://doi.org/10.1038/nn.3554>.
- Wake H, Moorhouse AJ, Miyamoto A, Nabekura J. Microglia: actively surveying and shaping neuronal circuit structure and function. *Trends Neurosci.* 2013;36:209–17. <https://doi.org/10.1016/j.tins.2012.11.007>.
- Healy LM, Perron G, Won S-Y, Michell-Robinson MA, Rezk A, Ludwin SK, et al. MerTK is a functional regulator of myelin phagocytosis by human myeloid cells. *J Immunol.* 2016;196:3375–84. <https://doi.org/10.4049/jimmunol.1502562>.
- Wu Y, Dissing-Olesen L, MacVicar BA, Stevens B. Microglia: dynamic mediators of synapse development and plasticity. *Trends Immunol.* 2015;36:605–13. <https://doi.org/10.1016/j.it.2015.08.008>.
- Wang C, Zhao C, Liu W, Huang X, Deng Y, Jiang J, et al. Depletion of microglia attenuates dendritic spine loss and neuronal apoptosis in the acute stage of moderate traumatic brain injury in mice. *J Neurotrauma.* 2020;37:43–54. <https://doi.org/10.1089/neu.2019.6460>.
- Matejuk A, Ransohoff RM. Crosstalk between astrocytes and microglia: an overview. *Front Immunol.* 2020;11. <https://doi.org/10.3389/fimmu.2020.01416>.
- Masuda T, Sankowski R, Staszewski O, Prinz M. Microglia heterogeneity in the single-cell era. *Cell Rep.* 2020;30:1271–81. <https://doi.org/10.1016/j.celrep.2020.01.010>.
- Nimmerjahn A, Kirchhoff F, Helmchen F. Neuroscience: resting microglial cells are highly dynamic surveillants of brain parenchyma in vivo. *Science.* 2005;308:1314–8. <https://doi.org/10.1126/science.1110647>.
- Paolicelli RC, Sierra A, Stevens B, Tremblay ME, Aguzzi A, Ajami B, et al. Microglia states and nomenclature: a field at its crossroads. *Neuron.* 2022;110:3458–83.
- Hansen DV, Hanson JE, Sheng M. Microglia in Alzheimer's disease. *J Cell Biol.* 2018;217:459–72. <https://doi.org/10.1083/jcb.201709069>.
- Lau SF, Fu AKY, Ip NY. Cytokine signaling convergence regulates the microglial state transition in Alzheimer's disease. *Cell Mol Life Sci.* 2021;78:4703–12. <https://doi.org/10.1007/s00018-021-03810-0>.
- Tzioras M, Daniels MJD, King D, Popovic K, Holloway RK, Stevenson AJ, et al. Altered synaptic ingestion by human microglia in Alzheimer's disease. *bioRxiv.* 2019. <https://doi.org/10.1101/795930>.
- Dani M, Wood M, Mizoguchi R, Fan Z, Walker Z, Morgan R, et al. Microglial activation correlates in vivo with both tau and amyloid in Alzheimer's disease. *Brain.* 2018. <https://doi.org/10.1093/brain/awy188>.
- Gomez-Nicola D, Boche D. Post-mortem analysis of neuroinflammatory changes in human Alzheimer's disease. *Alzheimers Res Ther.* 2015;7:42. <https://doi.org/10.1186/s13195-015-0126-1>.
- Janssen B, Vugts DJ, Funke U, Molenaar GT, Kruijer PS, van Berckel BNM, et al. Imaging of neuroinflammation in Alzheimer's disease, multiple sclerosis and stroke: Recent developments in positron emission tomography. *Biochim Biophys Acta Mol Basis Dis.* 2016;1862:425–41. <https://doi.org/10.1016/j.bbadis.2015.11.011>.
- Brown GC, Neher JJ. Eaten alive! Cell death by primary phagocytosis: 'Phagoptosis'. *Trends Biochem Sci.* 2012;37:325–32. <https://doi.org/10.1016/j.tibs.2012.05.002>.
- Selkoe DJ. Alzheimer's disease is a synaptic failure. *Science.* 2002;298:789–91. <https://doi.org/10.1126/science.1074069>.
- Selkoe DJ. Biochemistry and molecular biology of amyloid  $\beta$ -protein and the mechanism of Alzheimer's disease. *Handb Clin Neurol.* 2008;245–60. [https://doi.org/10.1016/S0072-9752\(07\)01223-7](https://doi.org/10.1016/S0072-9752(07)01223-7).
- Klein WL. Synaptic targeting by A $\beta$  oligomers (ADDLs) as a basis for memory loss in early Alzheimer's disease. *Alzheimer's Dementia.* 2006;2:43–55. <https://doi.org/10.1016/j.jalz.2005.11.003>.
- Müller-Schiffmann A, Herring A, Abdel-Hafiz L, Chepkova AN, Schäble S, Wedel D, et al. Amyloid- $\beta$  dimers in the absence of plaque pathology impair learning and synaptic plasticity. *Brain.* 2016;139:509–25. <https://doi.org/10.1093/brain/awv355>.
- Andrews SJ, Renton AE, Fulton-Howard B, Podlesny-Drabiniok A, Marcora E, Goate AM. The complex genetic architecture of Alzheimer's disease: novel insights and future directions. *EBioMedicine.* 2023;90:104511.
- Xu Z, Rao Y, Huang Y, Zhou T, Feng R, Xiong S, et al. Efficient strategies for microglia replacement in the central nervous system. *Cell Rep.* 2020;33:108443. <https://doi.org/10.1016/j.celrep.2020.108041>.
- Blue EE, Bis JC, Dorschner MO, Tsuang DW, Barral SM, Beecham G, et al. Genetic variation in genes underlying diverse dementias may explain a small proportion of cases in the Alzheimer's Disease Sequencing Project. *Dement Geriatr Cogn Disord.* 2018;45:1–17. <https://doi.org/10.1159/000485503>.
- Sassi C, Nalls MA, Ridge PG, Gibbs JR, Lupton MK, Troakes C, et al. Mendelian adult-onset leukodystrophy genes in Alzheimer's disease: critical influence of CSF1R and NOTCH3. *Neurobiol Aging.* 2018;66:179.e17–179.e29. <https://doi.org/10.1016/j.neurobiolaging.2018.01.015>.
- Giau VV, Senanarong V, Bagyinszky E, An SSA, Kim S. Analysis of 50 neurodegenerative genes in clinically diagnosed early-onset Alzheimer's disease. *Int J Mol Sci.* 2019;20:1514. <https://doi.org/10.3390/ijms20061514>.
- Chitu V, Biundo F, Shlager GGL, Park ES, Wang P, Guliniello ME, et al. Microglial homeostasis requires balanced CSF-1/CSF-2 receptor signaling. *Cell Rep.* 2020;30:3004–3019.e5. <https://doi.org/10.1016/j.celrep.2020.02.028>.
- Cannarile MA, Weisser M, Jacob W, Jegg AM, Ries CH, Rüttinger D. Colony-stimulating factor 1 receptor (CSF1R) inhibitors in cancer therapy. *J Immunother Cancer.* 2017;5:53. <https://doi.org/10.1186/s40425-017-0257-y>.
- Sosna J, Philipp S, Albay R, Reyes-Ruiz JM, Baglietto-Vargas D, LaFerla FM, et al. Early long-term administration of the CSF1R inhibitor PLX3397 ablates microglia and reduces accumulation of intraneuronal amyloid, neuritic plaque deposition and pre-fibrillar oligomers in 5XFAD mouse model of Alzheimer's disease. *Mol Neurodegener.* 2018;13:11. <https://doi.org/10.1186/s13024-018-0244-x>.
- Liu J, Chang L, Song Y, Li H, Wu Y. The role of NMDA receptors in Alzheimer's disease. *Front Neurosci.* 2019;13. <https://doi.org/10.3389/fnins.2019.00043>.
- Elmore MRP, Najafi AR, Koike MA, Dagher NN, Spangenberg EE, Rice RA, et al. Colony-stimulating factor 1 receptor signaling is necessary for microglia viability, unmasking a microglia progenitor cell in the adult brain. *Neuron.* 2014;82:380–97. <https://doi.org/10.1016/j.neuron.2014.02.040>.
- Chitu V, Stanley ER. Regulation of embryonic and postnatal development by the CSF-1 receptor. In: *Current topics in developmental biology.* 2017. p. 229–75. <https://doi.org/10.1016/bs.ctdb.2016.10.004>.
- Wang YQ, Berezovska O, Fedoroff S. Expression of colony stimulating factor-1 receptor (CSF-1R) by CNS neurons in mice. *J Neurosci Res.* 1999;57:616–32. [https://doi.org/10.1002/\(SICI\)1097-4547\(19990901\)57:53:0.CO;2-E](https://doi.org/10.1002/(SICI)1097-4547(19990901)57:53:0.CO;2-E).
- Nandi S, Gokhan S, Dai XM, Wei S, Enikolopov G, Lin H, et al. The CSF-1 receptor ligands IL-34 and CSF-1 exhibit distinct developmental brain expression patterns and regulate neural progenitor cell maintenance and maturation. *Dev Biol.* 2012;367:100–13. <https://doi.org/10.1016/j.ydbio.2012.03.026>.
- Luo J, Elwood F, Britschgi M, Villeda S, Zhang H, Ding Z, et al. Colony-stimulating factor 1 receptor (CSF1R) signaling in injured neurons facilitates protection and survival. *J Exp Med.* 2013;210:157–72. <https://doi.org/10.1084/jem.20120412>.
- Jin S, Sonobe Y, Kawanokuchi J, Horiuchi H, Cheng Y, Wang Y, et al. Interleukin-34 restores blood-brain barrier integrity by upregulating tight junction proteins in endothelial cells. *PLoS ONE.* 2014;9:e115981. <https://doi.org/10.1371/journal.pone.0115981>.
- Pons V, Lévesque P, Plante MM, Rivest S. Conditional genetic deletion of CSF1 receptor in microglia ameliorates the neuropathology of Alzheimer's disease. *Alzheimers Res Ther.* 2021;13:8. <https://doi.org/10.1186/s13195-020-00747-7>.
- Arreola MA, Soni N, Crapser JD, Hohnsfield LA, Elmore MRP, Matheos DP, et al. Microglial dyshomeostasis drives perineuronal net and synaptic loss in a CSF1R +/- mouse model of ALS, which can be rescued via CSF1R inhibitors. *Sci Adv.* 2021;7. <https://doi.org/10.1126/sciadv.abg1601>.
- Pons V, Laffamme N, Préfontaine P, Rivest S. Role of Macrophage Colony-Stimulating Factor Receptor on the Proliferation and Survival of Microglia Following Systemic Nerve and Cuprizone-Induced Injuries. *Front Immunol.* 2020;11. <https://doi.org/10.3389/fimmu.2020.00047>.
- Kiani Shabestari S, Morabito S, Danhash EP, McQuade A, Sanchez JR, Miyoshi E, et al. Absence of microglia promotes diverse pathologies and early lethality in Alzheimer's disease mice. *Cell Rep.* 2022;39:110961. <https://doi.org/10.1016/j.celrep.2022.110961>.

48. Cho S, Wood A, Bowlby M. Brain slices as models for neurodegenerative disease and screening platforms to identify novel therapeutics. *Curr Neuropharmacol*. 2007;5:19–33. <https://doi.org/10.2174/157015907780077105>.
49. Percie du Sert N, Hurst V, Ahluwalia A, Alam S, Avey MT, Baker M, et al. The ARRIVE guidelines 2.0: updated guidelines for reporting animal research. *BMJ Open Sci*. 2020;4:100115.
50. Mango D, Weisz F, Nisticò R. Ginkgolide acid protects against A $\beta$ -induced synaptic dysfunction in the hippocampus. *Front Pharmacol*. 2016;7. <https://doi.org/10.3389/fphar.2016.00401>.
51. Kobayashi K, Imagama S, Ohgomi T, Hirano K, Uchimura K, Sakamoto K, et al. Minocycline selectively inhibits M1 polarization of microglia. *Cell Death Dis*. 2013;4:e525. <https://doi.org/10.1038/cddis.2013.54>.
52. Tozzi A, Scip A, Tantucci M, de l'ure A, Ghiglieri V, Costa C, et al. Region- and age-dependent reductions of hippocampal long-term potentiation and NMDA to AMPA ratio in a genetic model of Alzheimer's disease. *Neurobiol Aging*. 2015;36:123–33. <https://doi.org/10.1016/j.neurobiolaging.2014.07.002>.
53. Galloway DA, Phillips AEM, Owen DRJ, Moore CS. Phagocytosis in the brain: Homeostasis and disease. *Front Immunol*. 2019;10. <https://doi.org/10.3389/fimmu.2019.00790>.
54. Nüsse O. Biochemistry of the phagosome: the challenge to study a transient organelle. *Sci World J*. 2011;11:2364–81.
55. Leyh J, Paeschke S, Mages B, Michalski D, Nowicki M, Bechmann I, et al. Classification of microglial morphological phenotypes using machine learning. *Front Cell Neurosci*. 2021;15. <https://doi.org/10.3389/fncel.2021.701673>.
56. Taylor SE, Morganti-Kossmann C, Lifshitz J, Ziebell JM. Rod microglia: a morphological definition. *PLoS ONE*. 2014;9:e97096. <https://doi.org/10.1371/journal.pone.0097096>.
57. Youmans KL, Tai LM, Kanekiyo T, Stine Jr WB, Michon SC, Nwabuisi-Heath E, et al. Intraneuronal A $\beta$  detection in 5xFAD mice by a new A $\beta$ -specific antibody. *Mol Neurodegener*. 2012;7:8. <https://doi.org/10.1186/1750-1326-7-8>.
58. Li S, Selkoe DJ. A mechanistic hypothesis for the impairment of synaptic plasticity by soluble A $\beta$  oligomers from Alzheimer's brain. *J Neurochem*. 2020;154:583–97. <https://doi.org/10.1111/jnc.15007>.
59. Liu Y, Given KS, Dickson EL, Owens GP, Macklin WB, Bennett JL. Concentration-dependent effects of CSF1R inhibitors on oligodendrocyte progenitor cells ex vivo and in vivo. *Exp Neurol*. 2019;318:32–41. <https://doi.org/10.1016/j.expneurol.2019.04.011>.
60. Willis EF, MacDonald KPA, Nguyen QH, Garrido AL, Gillespie ER, Harley SBR, et al. Repopulating microglia promote brain repair in an IL-6-dependent manner. *Cell*. 2020;180:833–846.e16. <https://doi.org/10.1016/j.cell.2020.02.013>.
61. Green KN, Crapser JD, Hohsfield LA. To kill a microglia: a case for CSF1R inhibitors. *Trends Immunol*. 2020;41:771–84. <https://doi.org/10.1016/j.it.2020.07.001>.
62. Jadhav VS, Lin PBC, Pennington T, Di Prisco GV, Jannu AJ, Xu G, et al. Trem2 Y38C mutation and loss of Trem2 impairs neuronal synapses in adult mice. *Mol Neurodegener*. 2020;15:62. <https://doi.org/10.1186/s13024-020-00409-0>.
63. Wright-Jin EC, Gutmann DH. Microglia as dynamic cellular mediators of brain function. *Trends Mol Med*. 2019;25:967–79. <https://doi.org/10.1016/j.molmed.2019.08.013>.
64. Li Q, Barres BA. Microglia and macrophages in brain homeostasis and disease. *Nat Rev Immunol*. 2018;18:225–42. <https://doi.org/10.1038/nri.2017.125>.
65. Graeber MB. Changing face of microglia. *Science*. 2010;330:783–8. <https://doi.org/10.1126/science.1190929>.
66. Sierra A, Encinas JM, Deudero JJP, Chancey JH, Enikolopov G, Overstreet-Wadiche LS, et al. Microglia shape adult hippocampal neurogenesis through apoptosis-coupled phagocytosis. *Cell Stem Cell*. 2010;7:483–95. <https://doi.org/10.1016/j.stem.2010.08.014>.
67. Lee JH, Kim J, Noh S, Lee H, Lee SY, Mun JY, et al. Astrocytes phagocytose adult hippocampal synapses for circuit homeostasis. *Nature*. 2021;590:612–7. <https://doi.org/10.1038/s41586-020-03060-3>.
68. Xu H, Gelyana E, Rajsombath M, Yang T, Li S, Selkoe D. Environmental enrichment potently prevents microglia-mediated neuroinflammation by human amyloid  $\beta$ -protein oligomers. *J Neurosci*. 2016;36:9041–56. <https://doi.org/10.1523/JNEUROSCI.1023-16.2016>.
69. Franco-Bocanegra DK, Gourari Y, McAuley C, Chatelet DS, Johnston DA, Nicoll JAR, et al. Microglial morphology in Alzheimer's disease and after A $\beta$  immunotherapy. *Sci Rep*. 2021;11:15955. <https://doi.org/10.1038/s41598-021-95535-0>.
70. Valero JG, Matas-Céspedes A, Arenas F, Rodriguez V, Carreras J, Serrat N, et al. The receptor of the colony-stimulating factor-1 (CSF-1R) is a novel prognostic factor and therapeutic target in follicular lymphoma. *Leukemia*. 2021;35:2635–49. <https://doi.org/10.1038/s41375-021-01201-9>.
71. Mancuso R, Fryatt G, Cleal M, Obst J, Pipi E, Monzón-Sandoval J, et al. CSF1R inhibitor JNJ-40346527 attenuates microglial proliferation and neurodegeneration in P301S mice. *Brain*. 2019;142:3243–64. <https://doi.org/10.1093/brain/awz241>.
72. Easley-Neal C, Foreman O, Sharma N, Zarrin AA, Weimer RM. CSF1R ligands IL-34 and CSF1 are differentially required for microglia development and maintenance in white and gray matter brain regions. *Front Immunol*. 2019;10. <https://doi.org/10.3389/fimmu.2019.02199>.
73. Hagan N, Kane JL, Grover D, Woodworth L, Madore C, Saleh J, et al. CSF1R signaling is a regulator of pathogenesis in progressive MS. *Cell Death Dis*. 2020;11:904. <https://doi.org/10.1038/s41419-020-03084-7>.
74. Olmos-Alonso A, Schetters STT, Sri S, Askew K, Mancuso R, Vargas-Caballero M, et al. Pharmacological targeting of CSF1R inhibits microglial proliferation and prevents the progression of Alzheimer's-like pathology. *Brain*. 2016;139:891–907. <https://doi.org/10.1093/brain/awv379>.
75. Hickman SE, Allison EK, El Khoury J. Microglial dysfunction and defective  $\beta$ -amyloid clearance pathways in aging Alzheimer's disease mice. *J Neurosci*. 2008;28:8354–60. <https://doi.org/10.1523/JNEUROSCI.0616-08.2008>.
76. Johnson NR, Yuan P, Castillo E, Lopez TP, Yue W, Bond A, et al. CSF1R inhibitors induce a sex-specific resilient microglial phenotype and functional rescue in a tauopathy mouse model. *Nat Commun*. 2023;14:118. <https://doi.org/10.1038/s41467-022-35753-w>.
77. Holloway OG, King AE, Ziebell JM. Microglia demonstrate local mixed inflammation and a defined morphological shift in an APP/PS1 mouse model. *J Alzheimers Dis*. 2020;77:1765–81. <https://doi.org/10.3233/JAD-200098>.
78. Bachstetter AD, Ighodaro ET, Hassoun Y, Aldeiri D, Neltner JH, Patel E, et al. Rod-shaped microglia morphology is associated with aging in 2 human autopsy series. *Neurobiol Aging*. 2017;52:98–105.
79. Wang L, Song G, Tan W, Qi M, Zhang L, Chan J, et al. miR-573 inhibits prostate cancer metastasis by regulating epithelial-mesenchymal transition. *Oncotarget*. 2015;6:35978–90. <https://doi.org/10.18632/oncotarget.5427>.
80. Tiwari S, Atluri V, Kaushik A, Yndart A, Nair M. Alzheimer's disease: pathogenesis, diagnostics, and therapeutics. *Int J Nanomed*. 2019;14:5541–54. <https://doi.org/10.2147/IJN.S200490>.
81. Nazere K, Takahashi T, Hara N, Muguruma K, Nakamori M, Yamazaki Y, et al. Amyloid beta is internalized via macropinocytosis, an HSPG- and lipid raft-dependent and Rac1-mediated process. *Front Mol Neurosci*. 2022;15. <https://doi.org/10.3389/fnmol.2022.804702>.
82. Wesén E, Jeffries GDM, Matson Dzebo M, Esbjörner EK. Endocytic uptake of monomeric amyloid- $\beta$  peptides is clathrin- and dynamin-independent and results in selective accumulation of A $\beta$ (1–42) compared to A $\beta$ (1–40). *Sci Rep*. 2017;7:2021. <https://doi.org/10.1038/s41598-017-02227-9>.
83. Mandrekar S, Jiang Q, Lee CYD, Koeningknecht-Talboo J, Holtzman DM, Landreth GE. Microglia mediate the clearance of soluble A $\beta$  through fluid phase macropinocytosis. *J Neurosci*. 2009;29:4252–62. <https://doi.org/10.1523/JNEUROSCI.5572-08.2009>.
84. Paasila PJ, Aramideh JA, Sutherland GT, Graeber MB. Synapses, Microglia, and Lipids in Alzheimer's Disease. *Front Neurosci*. 2022;15. <https://doi.org/10.3389/fnins.2021.778822>.
85. Zhou X, Jin G, Zhang J, Liu F. Recruitment mechanisms and therapeutic implications of tumor-associated macrophages in the glioma microenvironment. *Front Immunol*. 2023;14. <https://doi.org/10.3389/fimmu.2023.1067641>.
86. Mango D, Saidi A, Cisale GY, Feligioni M, Corbo M, Nisticò R. Targeting synaptic plasticity in experimental models of Alzheimer's disease. *Front Pharmacol*. 2019;10. <https://doi.org/10.3389/fphar.2019.00778>.
87. Nisticò R, Pignatelli M, Piccinin S, Mercuri NB, Collingridge G. Targeting synaptic dysfunction in Alzheimer's disease therapy. *Mol Neurobiol*. 2012;46:572–87.
88. Tijms BM, Vromen EM, Mjaavatten O, Holstege H, Reus LM, van der Lee S, et al. Cerebrospinal fluid proteomics in patients with Alzheimer's disease reveals five molecular subtypes with distinct genetic risk profiles. *Nat Aging*. 2024;4:33–47.
89. Spiteri AG, Wishart CL, Pamphlett R, Locatelli G, King NJC. Microglia and monocytes in inflammatory CNS disease: integrating phenotype and function. *Acta Neuropathol*. 2022;143:179–224.
90. Schafer ST, Mansour AA, Schlachetzki JCM, Pena M, Ghassemzadeh S, Mitchell L, et al. An in vivo neuroimmune organoid model to study human microglia phenotypes. *Cell*. 2023;186:2111–2126.e20.
91. Etebar F, Harkin DG, White AR, Dando SJ. Non-invasive in vivo imaging of brain and retinal microglia in neurodegenerative diseases. *Front Cell Neurosci*. 2024;18. <https://doi.org/10.3389/fncel.2024.1355557>.
92. Yang S, Qin C, Hu Z-W, Zhou L-Q, Yu H-H, Chen M, et al. Microglia reprogram metabolic profiles for phenotype and function changes in central nervous system. *Neurobiol Dis*. 2021;152:105290.
93. Li R-Y, Qin Q, Yang H-C, Wang Y-Y, Mi Y-X, Yin Y-S, et al. TREM2 in the pathogenesis of AD: a lipid metabolism regulator and potential metabolic therapeutic target. *Mol Neurodegener*. 2022;17:40.
94. Borst K, Schwabenland M, Prinz M. Microglia metabolism in health and disease. *Neurochem Int*. 2019;130:104331.
95. Hu B, Duan S, Wang Z, Li X, Zhou Y, Zhang X, et al. Insights into the role of CSF1R in the central nervous system and neurological disorders. *Front Aging Neurosci*. 2021;13. <https://doi.org/10.3389/fnagi.2021.789834>.



96. Han J, Chitu V, Stanley ER, Wszolek ZK, Karrenbauer VD, Harris RA. Inhibition of colony stimulating factor-1 receptor (CSF-1R) as a potential therapeutic strategy for neurodegenerative diseases: opportunities and challenges. *Cell Mol Life Sci.* 2022;79:219.
97. Neal ML, Fleming SM, Budge KM, Boyle AM, Kim C, Alam G, et al. Pharmacological inhibition of CSF1R by GW2580 reduces microglial proliferation and is protective against neuroinflammation and dopaminergic neurodegeneration. *FASEB J.* 2020;34:1679–94. <https://doi.org/10.1096/fj.201900567RR>.
98. Wang Y, Wernersbach I, Strehle J, Li S, Appel D, Klein M, et al. Early posttraumatic CSF1R inhibition via PLX3397 leads to time- and sex-dependent effects on inflammation and neuronal maintenance after traumatic brain injury in mice. *Brain Behav Immun.* 2022;106:49–66. <https://doi.org/10.1016/j.bbi.2022.07.164>.

## ACKNOWLEDGEMENTS

We kindly acknowledge A. Crevenna, Head of Imaging Facility of EMBL-Rome, for his kind assistance with confocal imaging tools.

## AUTHOR CONTRIBUTIONS

GP, VT and DM performed the experiments; NM and ADE helped with experiments and confocal imaging; GS helped with animal work and expertise; RN and VT conceived the study, DM and VT designed the research and interpreted data; RN, VT and DM wrote the manuscript.

## COMPETING INTERESTS

The authors declare no competing interests.

## ADDITIONAL INFORMATION

**Supplementary information** The online version contains supplementary material available at <https://doi.org/10.1038/s41398-024-03019-2>.

**Correspondence** and requests for materials should be addressed to Robert Nisticò, Viviana Triaca or Dalila Mango.

**Reprints and permission information** is available at <http://www.nature.com/reprints>

**Publisher's note** Springer Nature remains neutral with regard to jurisdictional claims in published maps and institutional affiliations.



**Open Access** This article is licensed under a Creative Commons Attribution-NonCommercial-NoDerivatives 4.0 International License, which permits any non-commercial use, sharing, distribution and reproduction in any medium or format, as long as you give appropriate credit to the original author(s) and the source, provide a link to the Creative Commons licence, and indicate if you modified the licensed material. You do not have permission under this licence to share adapted material derived from this article or parts of it. The images or other third party material in this article are included in the article's Creative Commons licence, unless indicated otherwise in a credit line to the material. If material is not included in the article's Creative Commons licence and your intended use is not permitted by statutory regulation or exceeds the permitted use, you will need to obtain permission directly from the copyright holder. To view a copy of this licence, visit <http://creativecommons.org/licenses/by-nc-nd/4.0/>.

© The Author(s) 2024